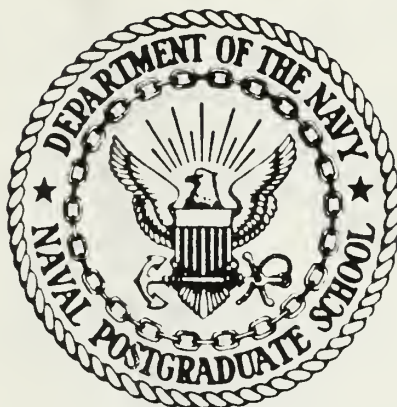


DUDLEY KNOX LIBRARY
NAVAL POSTGRADUATE SCHOOL
MONTEREY, CALIFORNIA 93943-5002

NAVAL POSTGRADUATE SCHOOL

Monterey, California



THESIS

DEVELOPING A PHYSICAL BASIS FOR AN AEROSOL
CLIMATOLOGY OF THE PACIFIC OCEAN

by

Frederick R. Pfeil

December 1986

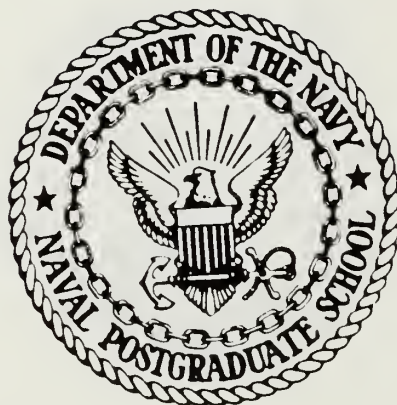
Thesis Advisor:

P. A. Durkee

Approved for public release; distribution is unlimited

T232211

NAVAL POSTGRADUATE Monterey, California



THESIS

DEVELOPING A PHYSICAL BASIS FOR
CLIMATOLOGY OF THE PACIFIC

by
Frederick R. Pfeil

December 1986

Thesis Advisor:

Approved for public release; distri

REPORT DOCUMENTATION PAGE

1a REPORT SECURITY CLASSIFICATION UNCLASSIFIED			1b RESTRICTIVE MARKINGS		
2a SECURITY CLASSIFICATION AUTHORITY			3 DISTRIBUTION/AVAILABILITY OF REPORT Approved for public release; distribution is unlimited		
2b DECLASSIFICATION/DOWNGRADING SCHEDULE			5 MONITORING ORGANIZATION REPORT NUMBER(S)		
4 PERFORMING ORGANIZATION REPORT NUMBER(S)			7a NAME OF MONITORING ORGANIZATION Naval Postgraduate School		
6a NAME OF PERFORMING ORGANIZATION Naval Postgraduate School		6b OFFICE SYMBOL (if applicable) 63	7b ADDRESS (City, State, and ZIP Code) Monterey, California 93943-5000		
6c ADDRESS (City, State, and ZIP Code) Monterey, California 93943-5000		9 PROCUREMENT INSTRUMENT IDENTIFICATION NUMBER			
8a NAME OF FUNDING/SPONSORING ORGANIZATION		8b OFFICE SYMBOL (if applicable)		10 SOURCE OF FUNDING NUMBERS	
8c ADDRESS (City, State, and ZIP Code)		PROGRAM ELEMENT NO		PROJECT NO	TASK NO
					WORK UNIT ACCESSION NO
11 TITLE (Include Security Classification) DEVELOPING A PHYSICAL BASIS FOR AN AEROSOL CLIMATOLOGY OF THE PACIFIC OCEAN					
12 PERSONAL AUTHOR(S) Pfeil, Frederick R.					
13a TYPE OF REPORT Master's Thesis		13b TIME COVERED FROM TO		14 DATE OF REPORT (Year, Month, Day) 1986 December	
15 PAGE COUNT 76					
16 SUPPLEMENTARY NOTATION					
17 COSATI CODES			18 SUBJECT TERMS (Continue on reverse if necessary and identify by block number)		
FIELD	GROUP	SUB-GROUP	aerosol, climatology, remote sensing		
19 ABSTRACT (Continue on reverse if necessary and identify by block number) NOAA-7 AVHRR data from April 1982 are used to demonstrate a method for building an aerosol climatology for the North and South Pacific Ocean. Sunlight is removed by deleting an area determined from visual inspection of many images. Red-visible (0.63 μ m), near-infrared (0.86 μ m) and infrared (11 μ m) channels, and the ratio of visible albedo to near-infrared albedo are used to eliminate areas of cloudiness. The ratio values are also used to indicate whether small (continental) or large (marine) aerosol particles predominate. Once a "clean" image of radiances due primarily to scattering by aerosols is obtained, satellite pixel values are averaged over one degree boxes from 50°N to 50°S, 110°E to 70°W. The mean visible and near-infrared albedos, mean ratio and standard deviations are computed and displayed as contoured fields over the North and South Pacific Ocean. These charts and individual examples are used to estimate spatial and temporal changes in aerosol concentration.					
20 DISTRIBUTION/AVAILABILITY OF ABSTRACT <input checked="" type="checkbox"/> UNCLASSIFIED/UNLIMITED <input type="checkbox"/> SAME AS RPT <input type="checkbox"/> DTIC USERS			21 ABSTRACT SECURITY CLASSIFICATION unclassified		
22a NAME OF RESPONSIBLE INDIVIDUAL Philip A. Durkee			22b TELEPHONE (Include Area Code) (408) 646-3465		22c OFFICE SYMBOL 63De

Approved for public release; distribution is unlimited.

Developing a Physical Basis for an Aerosol Climatology
of the Pacific Ocean

by

Frederick R. Pfeil
Lieutenant Commander, United States Navy
B.S., The Pennsylvania State University, 1976

Submitted in partial fulfillment of the
requirements for the degree of

MASTER OF SCIENCE IN METEOROLOGY AND OCEANOGRAPHY

from the

NAVAL POSTGRADUATE SCHOOL
December 1986

ABSTRACT

NOAA-7 AVHRR data from April 1982 are used to demonstrate a method for building an aerosol climatology for the North and South Pacific Ocean. Sunlint is removed by deleting an area determined from visual inspection of many images. Red-visible ($0.63\mu\text{m}$), near-infrared ($0.86\mu\text{m}$) and infrared ($11\mu\text{m}$) channels, and the ratio of visible albedo to near-infrared albedo are used to eliminate areas of cloudiness. The ratio values are also used to indicate whether small (continental) or large (marine) aerosol particles predominate. Once a "clean" image of radiances due primarily to scattering by aerosols is obtained, satellite pixel values are averaged over one degree boxes from 50°N to 50°S , 110°E to 70°W . The mean visible and near-infrared albedos, mean ratio and standard deviations are computed and displayed as contoured fields over the North and South Pacific Ocean. These charts and individual examples are used to estimate spatial and temporal changes in aerosol concentration.

TABLE OF CONTENTS

I.	INTRODUCTION	10
A.	BACKGROUND	11
B.	OBJECTIVES/MOTIVATION	12
C.	ORGANIZATION	13
II.	THEORY	14
A.	THE ELECTROMAGNETIC SPECTRUM	14
B.	THE RADIATIVE TRANSFER EQUATION	14
	1. Absorption and Scattering	14
	2. Angular Dependence	17
	3. The General RTE and Simplifying Assumptions	20
C.	ALBEDO AND RADIANCE	26
III.	DATA ANALYSIS	28
A.	SATELLITE AND DATA SET DESCRIPTION	28
B.	SUNGLINT AND CLOUD DETECTION	30
C.	STATISTICS	35
IV.	CONCLUSIONS AND RECOMMENDATIONS	69
	LIST OF REFERENCES	71
	INITIAL DISTRIBUTION LIST	74

LIST OF TABLES

1.	CORRELATION COEFFICIENTS FROM COMPARISON OF SATELLITE AND AEROSOL DEPENDENT TERMS IN EQN. 2.9	23
2.	SCATTERING COEFFICIENT AND SINGLE SCATTERING ALBEDO VS AEROSOL TYPE AND WAVELENGTH	25
3.	RAYLEIGH OPTICAL DEPTH, RADIANCE AND RATIOS	27
4.	AVHRR BANDWIDTHS FOR CHANNELS 1, 2 AND 4.	29
5.	REPRESENTATIVE CHANNEL 1/CHANNEL 2 RATIO VALUES FOR VARIOUS ATMOSPHERIC CONDITIONS	36

LIST OF FIGURES

2.1	Absorption bands of atmospheric gases, from Fleagle and Businger (1980)	15
2.2	The terms of Eqn. 2.3 as a function of radius: (a) πr^2 , (b) Q_{scat} , (c) dN/dr , (d) cumulative extinction	18
2.3	Single scattering phase function for the model of marine particles at 80% relative humidity after Shettle and Fenn (1979)	19
2.4	Relation of scattering, zenith, and azimuth angles, from Liou (1980)	21
3.1	NOAA-7 unenhanced AVHRR channel 1 image from 6 April 1982 covering the central Pacific ($\sim 175^\circ\text{W}$) from 50°N to 50°S , and the west coast of North America from 50°N to 30°N	31
3.2	Same as Fig. 3.1 with sunglint region deleted 40°N to 10°S , western half of image	32
3.3	Same as Fig. 3.1 with sunglint, land and cloud pixels deleted	33
3.4	Same as Fig. 3.1 with sunglint and clouds deleted based on channel 2 brightness value threshold test	34
3.5	Same as Fig. 3.1 with sunglint and clouds deleted based on channel 4 brightness value threshold and ratio value threshold tests	37
3.6	Same as Fig. 3.1 with all contaminant tests turned on: this image was included in climatological statistics-	38
3.7	Enlargement of a portion of Fig. 3.6: bright strip across center of image is haze	39
3.8	Number of pixels used in calculating statistics for 5-10 April 1982. Areas with greater than 1000 pixels are outlined	41
3.9	Number of pixels used in calculating statistics for 20-25 April 1982. Areas with greater than 1000 pixels are outlined	42
3.10	Number of pixels used in calculating statistics for 5-10 and 20-25 April 1982. Areas with greater than 1000 pixels are outlined	43
3.11	Mean channel 1 albedo for 5-10 April 1982. Albedos greater than 6.0% are outlined	44
3.12	Mean channel 1 albedo for 20-25 April 1982. Albedos greater than 6.0% are outlined	45
3.13	Mean channel 1 albedo for 5-10 and 20-25 April 1982. Albedos greater than 6.0% are outlined	46
3.14	Sea level pressure analysis for 12 GMT 05 April 1982	48
3.15	500 mb analysis for 12 GMT 05 April 1982	49
3.16	Channel 1 albedo standard deviation for 5-10 April 1982. Standard deviations greater than 1.5% are outlined	50

3.17	Channel 1 albedo standard deviation for 20-25 April 1982. Standard deviations greater than 1.5% are outlined	51
3.18	Channel 1 albedo standard deviation for 5-10 and 20-25 April 1982. Standard deviations greater than 1.5% are outlined	52
3.19	Mean channel 2 albedo for 5-10 April 1982. Albedos less than 2.0% and greater than 4.0% are outlined	53
3.20	Mean channel 2 albedo for 20-25 April 1982. Albedos less than 2.0% and greater than 4.0% are outlined	54
3.21	Mean channel 2 albedo for 5-10 and 20-25 April 1982. Albedos less than 2.0% and greater than 4.0% are outlined	55
3.22	Channel 2 albedo standard deviation for 5-10 April 1982. Standard deviations greater than 1.5% are outlined	57
3.23	Channel 2 albedo standard deviation for 20-25 April 1982. Standard deviations greater than 1.5% are outlined	58
3.24	Channel 2 albedo standard deviation for 5-10, 20-25 April 1982. Standard deviations greater than 1.5% are outlined	59
3.25	Mean channel 1/channel 2 ratios for 5-10 April 1982. Ratios greater than 1.6 are outlined	60
3.26	Mean channel 1/channel 2 ratios for 20-25 April 1982. Ratios greater than 1.6 are outlined	61
3.27	Mean channel 1/channel 2 ratios for 5-10 and 20-25 April 1982. Ratios greater than 1.6 are outlined	62
3.28	The El Chichon component of aerosol optical depth as a function of wavelength. Curves are labelled with station or latitude and date (from Dutton and DeLuisi, 1983)	65
3.29	Ratio standard deviation for 5-10 April 1982. Standard deviations greater than 0.2 are outlined	66
3.30	Ratio standard deviation for 20-25 April 1982. Standard deviations greater than 0.2 are outlined	67
3.31	Ratio standard deviation for 5-10 and 20-25 April 1982. Standard deviations greater than 0.2 are outlined-.....	68

LIST OF SYMBOLS

Symbol	Name
s	size parameter
r	particle radius
λ	radiation wavelength
m	complex refractive index
n	real part of m
v	imaginary part of m
β_{scat}	scattering coefficient
β_{abs}	absorption coefficient
β_{ext}	extinction coefficient
Q_{scat}	scattering efficiency
Q_{abs}	absorption efficiency
Q_{ext}	extinction efficiency
dN/dr	particle size distribution
τ	optical depth
ω_o	single scattering albedo
θ	satellite zenith angle
θ_o	solar zenith angle
φ	satellite azimuth angle
φ_o	solar azimuth angle
Ω	direction of upwelling beam
Ω_o	direction of upwelling beam
$p(\Omega, \Omega_o)$	scattering phase function
F_o	incoming solar radiance
L	upwelling diffuse radiance
α	albedo

ACKNOWLEDGEMENTS

Mr. Daniel Baldwin was very gracious and helpful during my stay at the National Center for Atmospheric Research, Boulder, Colorado. At that time the NOAA-7 data set was compiled, which Dr. James Coakley shared with me. Mr. Doug Burks' programming skills made the difficult and time-consuming task of processing the satellite data manageable. I appreciate his time and practical advice. Dr. Dennis W. Thomson carefully reviewed the manuscript and offered sound scientific and literary criticism. I would especially like to thank Dr. Philip A. Durkee for his encouragement throughout the thesis study. His enthusiasm and confidence in the worthiness of the project and in me were unflagging. And to my wife, Kathy, I offer my heartfelt gratitude for her enduring patience.

I. INTRODUCTION

Atmospheric aerosols scatter electromagnetic radiation over a broad spectrum of wavelengths, including those ranging from the visible (0.4 μm) to infrared (12 μm). Aerosol particles range in size from 0.001 μm to 100 μm , however a much smaller range, 0.1 μm to 10 μm ., most effectively contributes to the scattering of the visible radiation. Many of the physical characteristics of scattered radiation are parameterized in terms of the size parameter, s :

$$s = 2\pi r/\lambda. \quad (1.1)$$

For the wavelengths and particle sizes cited above, scattering by aerosols is significant for s values from approximately 0.05 to 160. The smallest s values occur with small particles and long wavelengths (Rayleigh scattering), whereas large s values (geometric optics for $s > \sim 20$) are obtained with large particles and short wavelengths. However, since most scattering occurs between the two extremes of particle size and wavelength, where s is on the order of one, analysis of the scattering requires application of Mie theory.

Atmospheric aerosols, depending on their chemistry, shape and size distribution, can be divided into two primary groups. Continental particles are composed mainly of silicates and carbon; marine particles are composed mostly of sea salt. Although the distribution of particles in the atmosphere at any place and time may be a combination of these types, continental distributions typically have many more small particles ($r \leq 1\mu\text{m}$) than marine distributions.

This thesis shows that an aerosol climatology can be built from satellite radiance data. Specifically, NOAA-7 Advanced Very High Resolution (AVHRR) data from April 1982 have been used to construct contoured fields of red-visible and near-infrared albedos, and the ratio of these albedos, as well as their standard deviations and the quantity of data used in the calculations. The procedures used to eliminate sunglint, land and clouds are also described.

A. BACKGROUND

As early as 1970 it was recognized that dust from Saharan storms could be detected over the North Atlantic Ocean in satellite images (Shenk and Curran, 1974). These dust clouds were mapped in 1979 with isopleths of optical depth from NOAA-3 data (Carlson, 1979). Less obvious background atmospheric aerosols were first seen as gray shades in Very High Resolution (VHR) visible images over water from Defense Meteorological Satellite Program (DMSP) satellites (Fett and Isaacs, 1979). Also, Earth Resources Technology Satellite One (ERTS-1) visible data were used to establish a linear upwelling radiance-aerosol optical depth relationship over water at $0.55\mu\text{m}$, $0.65\mu\text{m}$, and $0.75\mu\text{m}$ (Griggs, 1975). Optical depth was thus established to be one measure of aerosol concentration. Subsequent studies of data from different satellite sensors with higher spatial resolution have also confirmed that upwelling radiance and optical depth are nearly linearly related (Carlson and Wendling, 1977; Griggs, 1979; Durkee et al., 1986). Griggs (1983) concluded that the linear relationship can be used globally to monitor aerosol optical depth from satellite detected radiances. He also suggested that the aerosol size distribution could be inferred from a comparison of radiances from channel 1 ($0.63\mu\text{m}$) and channel 2 ($0.86\mu\text{m}$) of the AVHRR on NOAA-6. Takashima and Takayama (1983) used visible and infrared AVHRR data from NOAA-6 to estimate radiance variations resulting from sunglint and from ocean wave heights resulting from changing wind speed. In addition, they calculated radiation transmitted through the atmosphere in the visible and infrared spectral region, thereby accounting for absorption by atmospheric gases and scattering by aerosols.

Durkee (1984) showed how aerosol particle size variations affect satellite detected upwelling radiance. Since marine aerosol particles are produced by evaporating droplets from bursting seawater bubbles (Woodcock, 1953) and are therefore composed primarily of water soluble material, particle size is significantly affected by relative humidity changes (Hänel, 1976). As particle size increases, extinction increases, which implies that upwelling radiance should increase. Durkee (1984) verified this reasoning for a case study in southern California.

Meszaros and Vissy (1974) measured the concentration, size distribution and chemistry of aerosols over the Southern Ocean. Concentrations were less than those in the northern hemisphere for all sizes. The size distribution ranged between $0.03\mu\text{m}$ and $64.0\mu\text{m}$, with a maximum near $0.1\mu\text{m}$. The particles were mainly sea salt and sulphur compounds. These results defined a background aerosol, undisturbed by land sources.

B. OBJECTIVES/MOTIVATION

In this thesis the relationship between satellite detected upwelling radiance and optical depth is used to establish the physical basis for an aerosol climatology of the North and South Pacific Ocean. Brightness counts from channel 1 and channel 2 of the AVHRR are converted to albedos using calibration algorithms provided by NOAA (Kidwell, 1984). Combinations of these values are averaged in 1° squares over the entire basin. These average values are then used to build a data base for the North and South Pacific Ocean. The data used to demonstrate the method were AVHRR measurements from April 1982.

A bias toward fair weather radiance values is anticipated because cloudy portions of the satellite pass have been excluded. Aerosol particles in cloudy regions, which have water-saturated air, act as condensation nuclei and thus the aerosol can grow rapidly to cloud droplet size. The size distribution of this study's data sample may be different from that of the North and South Pacific Ocean, cloudy and cloud-free. The data must be interpreted accordingly.

The ratio of albedo at channel 1 to albedo at channel 2 is also averaged in 1° squares over the North and South Pacific Ocean. Ratios of albedos at different wavelengths vary as the aerosol particle concentration varies. Durkee (1984) and Bulfinch (1986) showed that as the relative concentration of smaller particles increase, the ratio values of AVHRR channel 1 albedo/channel 2 albedo increase. Therefore horizontal variations in ratio values indicate horizontal variations in size distribution, with large ratio values indicating more small ($r < 1\mu\text{m}$) particles and a more continental distribution type.

If the climatological background aerosol concentration over the North and South Pacific Ocean is known, it should be straightforward to detect changes in aerosol size distribution and composition resulting from an intrusion of continental aerosol particles into the troposphere over the Pacific Ocean. Iwasaka et al. (1983) studied an Asian dust storm which occurred in April 1979. Ground based measurements of the aerosol particles yielded a representative size distribution function and extinction coefficient. These data, as well as a Japanese Geosynchronous Meteorological Satellite visible image clearly showing the dust cloud, indicate that Asian dust events moving over the North Pacific Ocean are similar to Saharan dust storms which move over the North Atlantic Ocean (Carlson and Wendling, 1977; Carlson, 1979; Norton, et al., 1980; Shenk and Curran, 1974). A case study will be presented which documents an

event in the eastern North Pacific Ocean that may be related to the eruption of El Chichón, Mexico in March-April 1982. The ability to identify and track these clouds across the North Pacific Ocean may lead to improved forecasts of electro-optical system performance and improved visibility forecasts. The climatological data have important applications to climate studies due to the dust particles' role in cloud physics and radiative transfer processes. Furthermore, this information bears directly on chemical oceanography because the dust can be carried over a large area and can contribute significantly to deep ocean sedimentation (Iwasaka, et al., 1983).

C. ORGANIZATION

Chapter 2 will discuss the theory of radiative scattering by atmospheric aerosols, the basic equations of radiative transfer and the assumptions applied to simplify them. The data set and acquisition equipment are described in Chapter 3, as is the procedure used to remove contaminants (sunglint and clouds). Since the objective is an aerosol climatology, it must be established that only radiation scattered by aerosols is being sensed by the instrument, not by other atmospheric constituents or phenomena. A case study of one area in the North Pacific Ocean is given, with an example of the contaminant discriminating process. Conclusions and recommendations for future study are stated in Chapter 4.

II. THEORY

A. THE ELECTROMAGNETIC SPECTRUM

For remote sensing of aerosols, we detect the interaction of visible and near-infrared radiation with aerosol particles dispersed in air. This is called the inverse problem; i.e., information about the particles doing the scattering is inferred from an analysis of the field of scattered radiation (Bohren and Huffman, 1983).

The radiation detected by a satellite sensor has been scattered by air molecules, aerosol particles suspended in the air and the earth's surface. Molecular scattering is described by Rayleigh theory ($s < 1$). Molecular scattering makes up a significant portion of the total atmospheric scattering, but, as will be discussed below, does not vary significantly with position. At red visible and near-infrared wavelengths, reflectance by an ocean surface is very small (Ramsey, 1968). Therefore any variation in the radiation field is primarily due to aerosol scattering. Mie theory describes aerosol scattering ($s \sim 1$). The radiation field is affected by the size and number of particles present, and their chemistry. All of these vary significantly in the horizontal due to their sources.

B. THE RADIATIVE TRANSFER EQUATION

The radiative transfer equation (RTE) can be used to completely describe the radiation field at a satellite sensor, accounting for attenuation (absorption, scattering and reflection out of the field of view) and intensification (emission, and scattering and reflection into the field of view).

1. Absorption and Scattering

Atmospheric gases have absorption bands which, when combined, give the resultant absorption spectrum of the earth's atmosphere (see Fig. 2.1). Some sensors, such as the human eye, are "designed" to take advantage of the "windows" where the solar radiance is absorbed least; that is, where the sun's energy is able to penetrate the atmosphere. In the window regions the radiation can also be scattered back toward the sensor by gas molecules, cloud droplets, aerosols, or the earth's surface (land or sea). AVHRR channel 1, at $0.55\mu\text{m}$ to $0.68\mu\text{m}$, and channel 2, at $0.70\mu\text{m}$ to $1.00\mu\text{m}$, span two of the atmosphere's absorption windows.

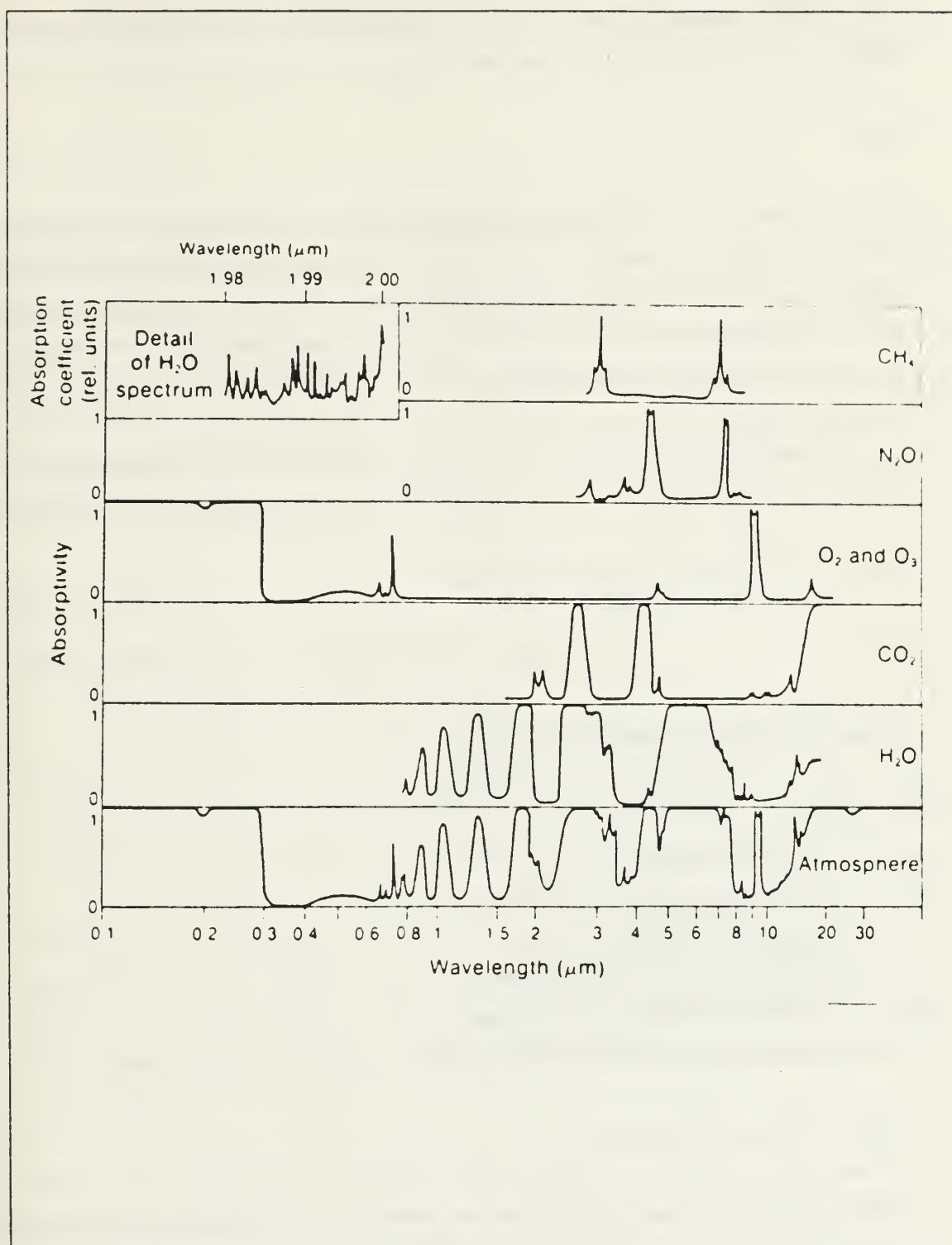


Fig. 2.1 Absorption bands of atmospheric gases, from Fleagle and Businger (1980).

The complex refractive index represents both the scattering and absorbing ability of a substance. It is defined as:

$$m = n + iv. \quad (2.1)$$

The real part, n , is the ratio of the speed of light in one substance to that in another; the magnitude of scattering is partially governed by the magnitude of n . The imaginary part, v , is a measure of the absorptivity of a substance. Wavelength strongly affects v , but v is no larger than 10^{-4} for wavelengths less than $1\mu\text{m}$ (Shettle and Fenn, 1979); therefore, there is little absorption by aerosols of the radiation sensed by AVHRR channels 1 and 2.

Scattering by aerosols is described using the scattering coefficient, β_{scat} ; extinction is given by the extinction coefficient, β_{ext} (see Bohren and Huffman, 1983):

$$\beta_{\text{scat}} = \int_0^\infty \pi r^2 Q_{\text{scat}}(m,r) \{dN(r)/dr\} dr \quad (2.2)$$

and

$$\beta_{\text{ext}} = \int_0^\infty \pi r^2 Q_{\text{ext}}(m,r) \{dN(r)/dr\} dr, \quad (2.3)$$

where

- r = particle radius,
- m = complex refractive index,
- Q_{scat} = scattering efficiency,
- Q_{ext} = extinction efficiency and
- $dN(r)/dr$ = particle size distribution.

The scattering and extinction coefficients are related in the following way:

$$\beta_{\text{ext}} = \beta_{\text{abs}} + \beta_{\text{scat}}. \quad (2.4)$$

Therefore the atmospheric scattering and extinction of aerosols is the vertical sum through the atmosphere of the product of three terms: the cross sectional area of the particles (πr^2), the scattering or extinction efficiency (Q_{scat} , Q_{ext}), and the size distribution (dN/dr). Fig. 2.2 illustrates the variation of these terms with radius. The

relative magnitudes of these terms determines the magnitude of the extinction coefficient which in turn gives the optical depth, defined as:

$$\tau = \int_0^H \beta_{\text{ext}} dz, \quad (2.5)$$

where H is the height of the satellite. It can be seen from Fig. 2.2 that when r is small, πr^2 and Q_{ext} are small while dN/dr is large; when r is large, πr^2 is large, and dN/dr and Q_{ext} become small. The result is that β_{ext} is affected by a bounded region of particle sizes. For visible wavelengths and a marine aerosol size distribution model at 80% relative humidity this range is from approximately $0.5\mu\text{m}$ to $5.0\mu\text{m}$ (Durkee, 1984). Because the imaginary part of the complex index of refraction is so small at these wavelengths ($v \sim 10^{-4}$), $\beta_{\text{scat}} \sim \beta_{\text{ext}}$. This means that marine aerosols are efficient scatterers. The ratio:

$$\omega_o = \beta_{\text{scat}}/\beta_{\text{ext}}, \quad (2.6)$$

called the single scattering albedo, is approximately 1 in this case.

2. Angular Dependence

The scattering phase function, $p(\Omega, \Omega_o)$, describes the angular dependence of scattering. If we assume the particles are spherical (necessary to get an exact solution to Maxwell's equations for electromagnetic waves, and one which is essential to keep the problem computationally tractable), Mie theory can be used to calculate $p(\Omega, \Omega_o)$. For a complete description, see Bohren and Huffman, 1983. Fig. 2.3 shows the phase function calculated from Mie theory at 80% relative humidity. Marine aerosols can be assumed spherical if the relative humidity is high, because they are hygroscopic and therefore tend toward spheres as they gain water on their surface. For the marine aerosol at 80% relative humidity, particles primarily scatter forward (Shettle and Fenn, 1979).

The albedo of the ocean surface is nearly zero in the red-visual to near-infrared region of the spectrum (Ramsey, 1968), but sunglint is observed because specular reflection occurs off wave facets oriented such that incoming solar radiation is reflected into the sensor's view. The size of the sunglint area increases as the wind velocity increases (Cox and Munk, 1954).

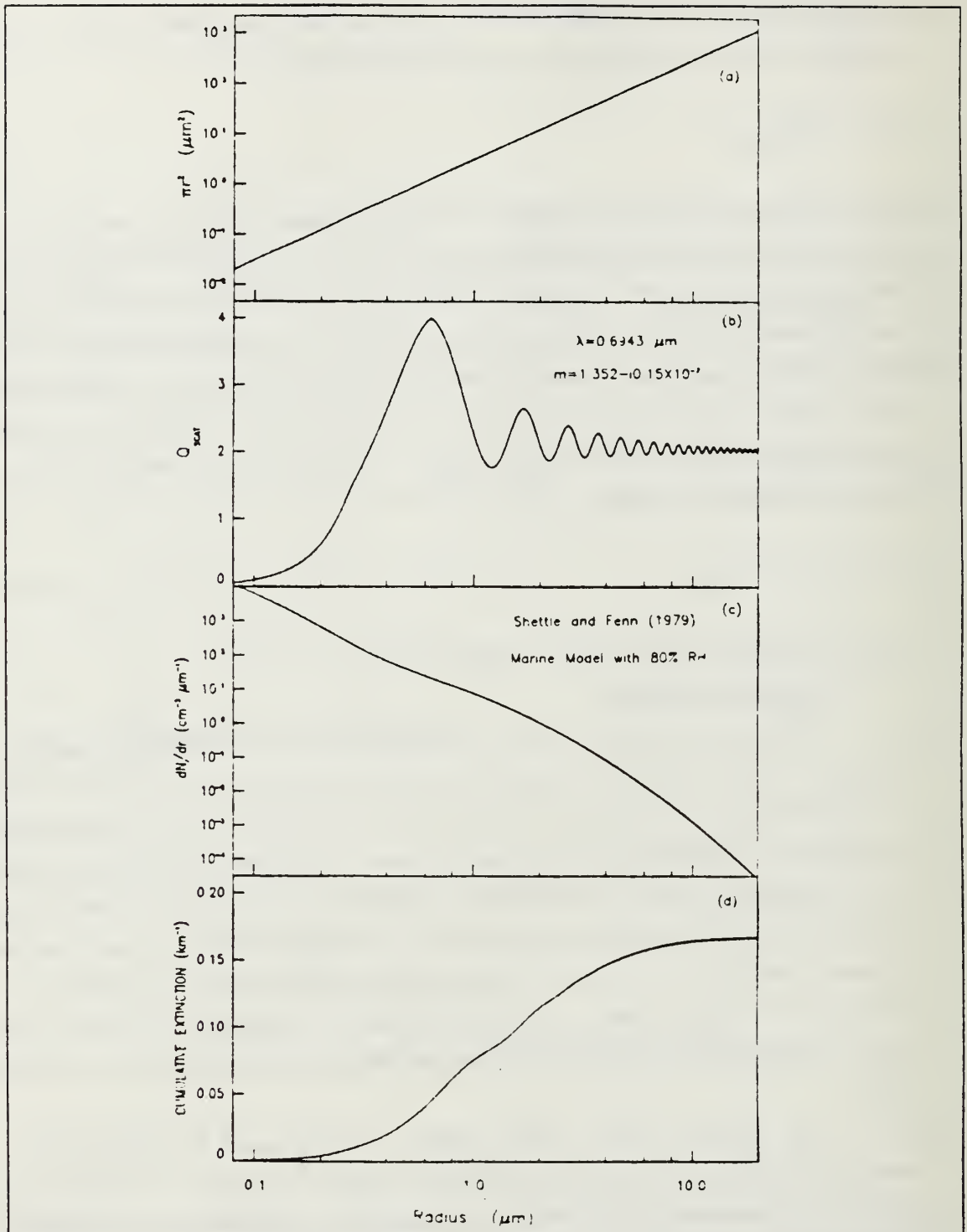


Fig. 2.2 The terms of Eqn. 2.3 as a function of radius:
 (a) πr^2 , (b) Q_{scat} , (c) dN/dr ,
 (d) cumulative extinction.

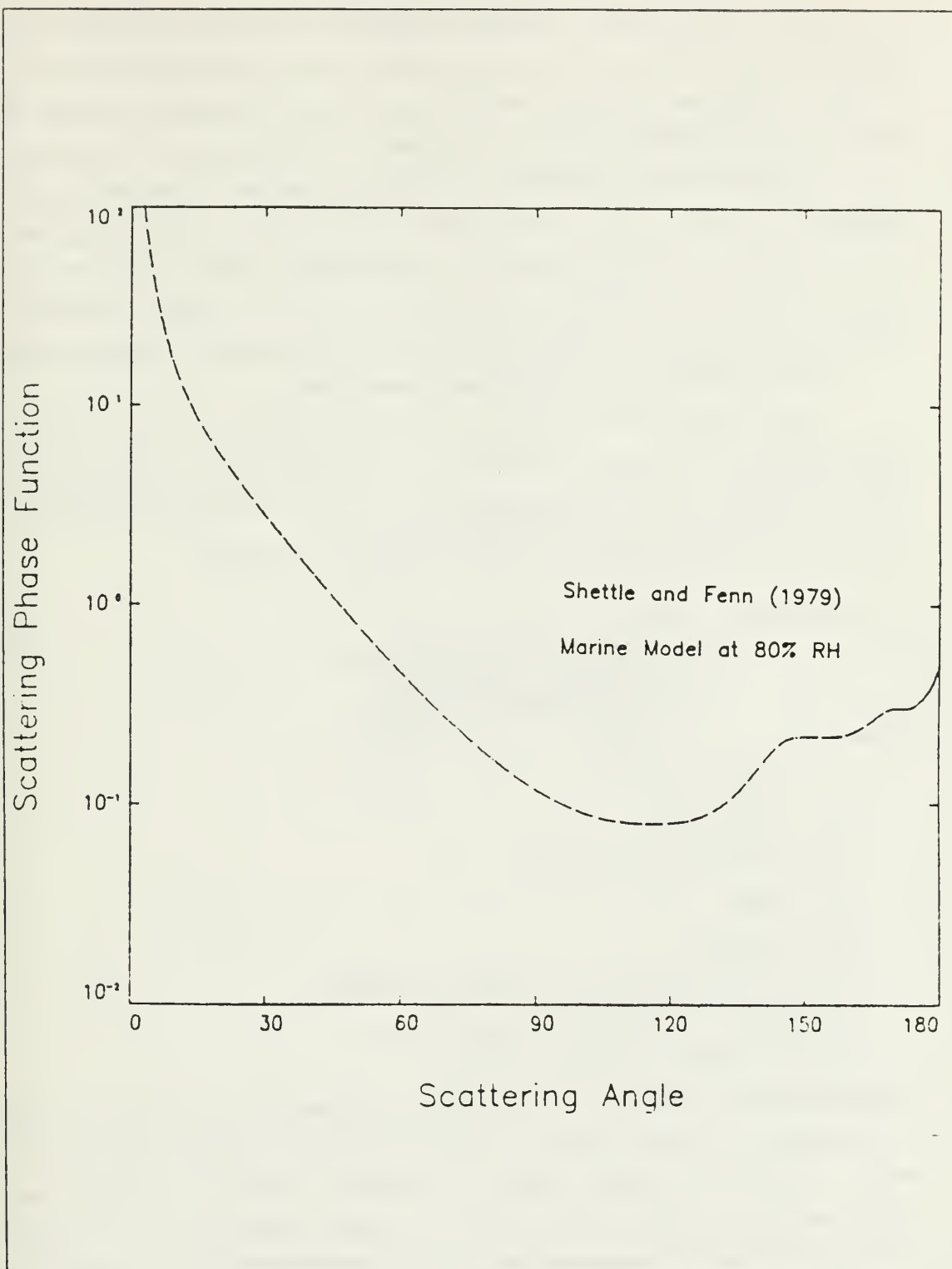


Fig. 2.3 Single scattering phase function for the model of marine particles at 80% relative humidity after Shettle and Fenn (1979).

Due to the angular dependence of particle scattering and surface reflectance, the RTE depends on sun-earth-satellite geometry. Fig. 2.4 identifies all of the angles involved. These are important because the amount of radiation received by the satellite sensor depends on the view direction of the sensor. The intensity detected varies with the observing zenith (θ) and azimuth (ϕ) angles. If the upwelling radiance depends on reflection of solar radiation, solar zenith (θ_o) and azimuth (ϕ_o) must also be accounted for. The angle between the incoming solar beam and the beam received at the sensor (α) is a function of these four angles. The angular direction of the upwelling beam described by (θ, ϕ) is called Ω and that described by (θ_o, ϕ_o) is Ω_o .

3. The General RTE and Simplifying Assumptions

We can now write the RTE. A basic assumption is that the atmosphere is plane parallel; i.e., the top and bottom of the atmosphere are two parallel planes. If optical properties of the atmosphere are assumed to be horizontally homogeneous, the general form of the RTE is given by (see for example Liou, 1980):

$$\begin{aligned} \mu dL(\tau, \Omega)/d\tau = & L(\tau, \Omega) \\ & - (\omega_o/4\pi) \int_{4\pi} L(\tau, \Omega') p(\Omega, \Omega') d\Omega' \\ & - (\omega_o/4\pi) \pi F_o p(\Omega, -\Omega_o) e^{-\tau/\mu_o}, \end{aligned} \quad (2.7)$$

where

L = diffuse radiance,

τ = optical depth,

ω_o = single scattering albedo,

$\mu = \cos\theta$,

$\mu_o = \cos\theta_o$,

Ω = angular direction of upwelling beam (θ, ϕ),

$p(\Omega, \Omega_o)$ = scattering phase function and

πF_o = incoming solar radiative flux.

The first term on the right hand side describes attenuation of the beam by absorption or scattering; the second accounts for intensification by multiple scattering into the beam in the following sense. $L(\tau, \Omega')$ is the diffuse radiation from all directions; $p(\Omega, \Omega')$ accounts for the part of L which has been scattered into the viewing angle, and $\omega_o/4\pi$ accounts for the absorption of L scattered into the viewing angle. The third term is the intensification by single scattering; that is, the solar irradiance which is directly scattered toward the sensor.

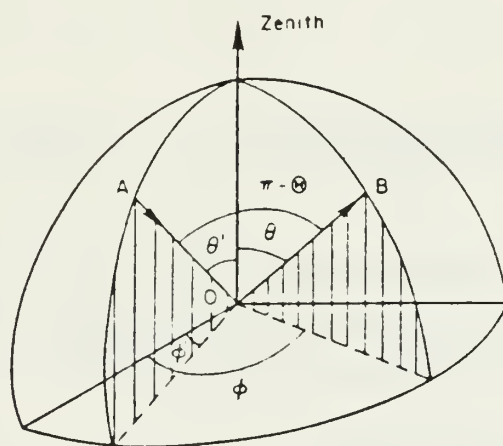


Fig. 2.4 Relation of scattering, zenith, and azimuth angles, from Liou (1980).

The multiple scattering term is difficult to evaluate because the intensity field must be integrated over all directions. It is reasonable to make a single scattering approximation if the optical depth is small and the mean free path between aerosol particles is large. Global values of optical depth range from 3.0 for a boundary layer with heavy haze to 0.003 for the troposphere (World Climate Research Programme, 1986). Typically, the aerosol optical depth over the ocean is less than 0.2. Therefore it is assumed that aerosol particles are randomly distributed in air, the number of particles is small and their separation is large, so that single scattering of radiation dominates. Also, the upward intensity at the bottom of the atmosphere is assumed to be zero ($L(\tau_1; \mu, \varphi) = 0$). The RTE for an atmosphere with total optical depth of τ_1 is then:

$$L(0; \mu, \varphi) = \{\omega_0 \mu_0 F_0 / 4(\mu + \mu_0)\} p(\Theta) \{1 - \exp(-\tau_1(1/\mu + 1/\mu_0))\}, \quad (2.8)$$

where Θ is the single scattering angle. For an optically thin atmosphere $\tau_1(1/\mu + 1/\mu_0) < 1$; for example, given $\tau = 0.04$ and $\theta, \theta_0 = 10^\circ$ ($\mu, \mu_0 = 0.985$), $\tau_1(1/\mu + 1/\mu_0) = 0.08$. Then, the RTE reduces to:

$$L(0; \mu, \varphi) \sim (\omega_0 F_0 / 4\mu) p(\Theta) \tau_1, \quad (2.9)$$

which says that the reflected intensity from single scattering in an optically thin atmosphere is a nearly linear function of τ_1 . Since $\omega_0 \sim 1$, the slope depends on the scattering phase function and the satellite viewing geometry. Durkee (1984) calculated correlation coefficients for various combinations of terms in equation 2.9 (see Table 1). The largest improvement in the coefficient, indicating increased precision, resulted from the addition of μ , indicating the satellite viewing geometry is the most important information for accurately describing the relationship between L and τ .

Table 2 shows the variation of scattering coefficient (β_{scat}) and single scattering albedo (ω_0) with wavelength for the marine, rural and urban aerosol models of Shettle and Fenn (1979). It is to be recalled that Fig. 2.3 shows the variation of phase function $p(\Theta)$ with wavelength. It is clear that β_{scat} and ω_0 (and, therefore, τ) vary more with wavelength for rural and urban aerosols than for marine aerosols.

TABLE 1
CORRELATION COEFFICIENTS FROM COMPARISON OF
SATELLITE
AND AEROSOL DEPENDENT TERMS IN EQN. 2.9

Terms compared	Correlation coefficient
L vs τ	0.11
$4\mu L/F_0$ vs τ	0.56
$4\mu L/F_0$ vs $p(\Theta)\tau$	0.67

There is little variation in $p(\Theta)$. The result is that ω_o and τ are larger at red-visible than at near-infrared wavelengths for rural and urban aerosols; but they are relatively constant for marine aerosols.

Using equation 2.9 for two wavelengths, a ratio can be formed:

$$L_{\text{red}}/L_{\text{NIR}} \sim ((\omega_o F_o / 4\mu)p(\Theta)\tau)_{\text{red}} / ((\omega_o F_o / 4\mu)p(\Theta)\tau)_{\text{NIR}}. \quad (2.10)$$

The right hand side will be larger for continental aerosol types (rural and urban) than for marine aerosols and, therefore, ratios of radiance at those wavelengths will be also.

Eqn. 2.10 describes the ratio for aerosol radiance. The total diffuse radiance, L , is the sum of radiance due to Rayleigh scattering, L_R , and radiance due to aerosol scattering, L_A . Therefore the ratio in Eqn. 2.10 can be expressed as:

$$L_{\text{red}}/L_{\text{NIR}} = (L_A + L_R)_{\text{red}} / (L_A + L_R)_{\text{NIR}}. \quad (2.11)$$

The relative importance of Rayleigh scattering was estimated by calculating Rayleigh radiance values at $0.63\mu\text{m}$ and $0.86\mu\text{m}$. Climatological April atmospheric profiles at 50°N , the equator, and 50°S were used to estimate variation in Rayleigh optical depth (McCartney, 1976). Rayleigh radiance was then calculated for various sun-earth-satellite geometries. Table 3 shows the values obtained. Notice how small the optical depth variation is with latitude and how little the ratios vary with latitude or geometry.

The ratio of Rayleigh optical depths indicates that if few aerosols are present the ratio values should be 3. Since the ratio varies so little in a purely Rayleigh atmosphere, the magnitude of (2.11) depends on the spectral variation of L_A . To calculate a correct ratio of aerosol radiance it is therefore necessary to estimate the Rayleigh contribution, L_R . In this study the Rayleigh radiance was not explicitly removed from the satellite-measured radiance. However, regions with radiance much above the Rayleigh radiance (see Table 3) are dominated by aerosol scattering. Therefore, where L is significantly larger than L_R the ratio is presumed to be a good indicator of aerosol type.

TABLE 2
SCATTERING COEFFICIENT AND SINGLE SCATTERING ALBEDO
VS AEROSOL TYPE AND WAVELENGTH

		50% RH		80% RH
	λ	Rural	Urban	Marine
β_{scat}	0.694	0.106	0.091	0.207
	1.06	0.050	0.049	0.191
ω	0.694	0.934	0.635	0.994
	1.06	0.865	0.567	0.992

C. ALBEDO AND RADIANCE

Albedo is defined as the ratio of outgoing radiance to incoming radiance; i.e.,

$$\alpha = L/F_o, \quad (2.12)$$

and is usually expressed as a percentage. The ratio of albedos at two different wavelengths is directly proportional to the ratio of outgoing radiance and, for the optically thin plane parallel atmosphere, to the optical depth. NOAA AVHRR radiometer brightness counts can be directly transformed into albedos using linear relationships derived in pre-flight calibrations (Kidwell, 1984). Therefore, the results presented here are in terms of an albedo derived from the NOAA-7 AVHRR measurements.

TABLE 3
RAYLEIGH OPTICAL DEPTH, RADIANCE AND RATIOS

τ_R	τ_R	θ	θ_o	φ	α	L_{red}	L_{NIR}	L_{red}/L_{NIR}
50N								
.0591	.0197	10	10	0	1.9903	1.0319	0.2446	4.2187
		10	10	180	1.8777	0.9735	0.2305	4.2234
		40	40	0	2.4783	1.2849	0.3127	4.1091
		40	40	180	1.3150	0.6818	0.1625	4.1957
$\tau_R/\tau_R = 3.0000$								
Equator								
.0559	.0186	10	10	0	1.8836	0.9766	0.2312	4.2240
		10	10	180	1.7770	0.9213	0.2178	4.2300
		40	40	0	2.3475	1.2171	0.2957	4.1160
		40	40	180	1.2439	0.6449	0.1536	4.1986
$\tau_R/\tau_R = 3.0054$								
50S								
.0585	.0195	10	10	0	1.9701	1.0214	0.2420	4.2207
		10	10	180	1.8586	0.9636	0.2280	4.2263
		40	40	0	2.4534	1.2720	0.3094	4.1112
		40	40	180	1.3015	0.6748	0.1608	4.1965
$\tau_R/\tau_R = 3.0000$								

III. DATA ANALYSIS

A. SATELLITE AND DATA SET DESCRIPTION

The data set used in this thesis was obtained using NOAA-7, a sun-synchronous polar orbiting satellite at a nominal altitude of 833 km. It crosses the equator at approximately 0230 (ascending; northbound crossing) and 1430 (descending; southbound crossing) Local Standard Time. Back scattered radiance is detected with the Advanced Very High Resolution Radiometer (AVHRR), a cross-track scanning system, in five bands of the solar spectrum called channels. Channels 1 ($0.65\mu\text{m}$), 2 ($0.85\mu\text{m}$), and 4 ($11.0\mu\text{m}$) were used in this study. The bandwidths of these three channels are given in Table 4. The data have a satellite subpoint resolution of 1.1 km.

Although there is a water vapor absorption band at $0.94\mu\text{m}$ and, therefore, in the channel 2 band, its effect on the ratio is slight (Durkee, 1984). A decrease in water vapor absorption, as would occur over land, would increase channel 2 albedo, and therefore decrease the ratio. An increase in water vapor absorption, indicative of a more marine environment, would decrease channel 2 albedo, and thus increase the ratio. But in a marine environment the increased relative humidity would increase the the number of large particles in the size distribution. The channel 2 albedo would then increase more than the channel 1 albedo, thus decreasing the ratio. In this study it is assumed that these opposing effects cancel.

A reduced resolution subset of the AVHRR data was used to do the calculations on a VAX11/780 computer. An onboard satellite processor samples four of every five picture elements (called pixels) along the scan line to compute an average value. The data are further sampled by using every third scan line. This leads to an effective subpoint resolution of 4 km by 3.3 km. The particular data used here were copied from a larger set at the National Center for Atmospheric Research (NCAR), Boulder, Colorado. Data were recorded for six consecutive days, followed by a ten-day lapse, and then a second six-day period. The dates were 5-10 and 20-25 April 1982. The data set was restricted to the Pacific Ocean (50°N - 50°S , 110°E - 70°W). Since each pass was nominally thirty degrees wide it took seven passes to cover the Pacific Ocean. There was some overlap of successive passes.

TABLE 4
AVHRR BANDWIDTHS FOR CHANNELS 1, 2 AND 4.

Channel	Bandwidth(μm)
1	0.58-0.68
2	0.725-1.10
4	10.5-11.3

The AVHRR was pre-flight calibrated such that a linear relationship between brightness counts and percent albedo for both channels 1 and 2 was known. Slope and intercept values are part of the source data stream from the AVHRR; thus, it was a simple procedure to convert channel 1 and 2 brightness counts to albedo percentages and to form their ratio.

B. SUNGLINT AND CLOUD DETECTION

The data were checked in various ways to ascertain that the data would be representative of aerosol concentration only, and not contaminated by other effects. A particularly spectacular case where a haze layer was visible in channel 1 will be used to illustrate these checks. Fig. 3.1 shows the channel 1 image. The NCAR data set had more than one satellite pass on each file. Notice that two passes are appended and the image changes three-fourths of the way through. The first part is the mid-Pacific Ocean, approximately 175°W from 35°N to 50°S. The last part is the west coast of North America from 50°N to 30°N. Sun glint is a serious contaminant of channel 1 and channel 2, but is easily detected. The sun glint is a function of viewing geometry and sea state. Since the daylight orbits were near 1430 LST the geometry dictated that the glint would always be on the western edge of the image. Thus the sea state determined the degree of broadness of the glint region. After visual examination of many images, a conservative approach required that the entire western half of the pass between 40°N and 10°S be deleted. Fig. 3.2 shows an image with the sun glint region deleted.

The ratio of channel 1 to channel 2 albedo proved useful in two ways. Vegetation has a high near-infrared reflectance so upwelling radiance from land should be greater at near-infrared than at visible wavelengths. Therefore ratio values over land should be smaller than over water, and were in fact less than 1.0. Fig. 3.3 shows the west coast of the U.S. deleted, at least where there is no cloudiness. Vancouver Island, British Columbia is labelled for reference. This ratio was also one of several checks used to identify small cumulus clouds and is discussed further below.

Three checks were used to screen out clouds. First, channel 2 images were visually inspected to determine a threshold value above which it was certain there were clouds present. This check was good at eliminating thick (therefore highly reflective) low, middle and upper-level clouds, but it did not eliminate thin cirrus or small fair weather cumulus. Fig. 3.4 has pixels above the chosen threshold deleted.

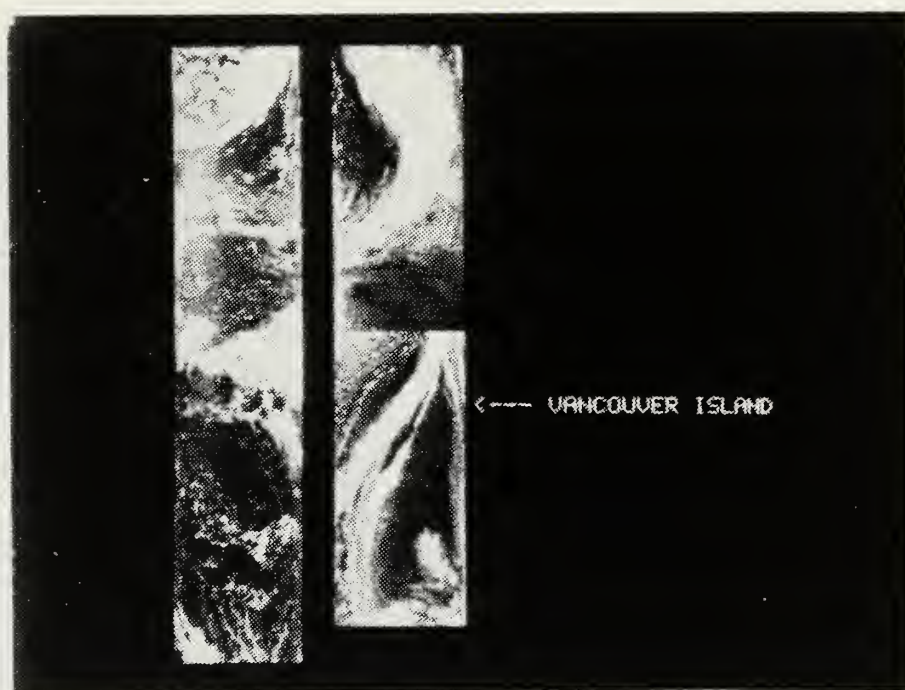


Fig. 3.1 NOAA-7 unenhanced AVHRR channel 1 image from
6 April 1982 covering the central Pacific ($\sim 175^\circ\text{W}$)
from 50°N to 50°S , and the west coast of North America from 50°N to 30°N .

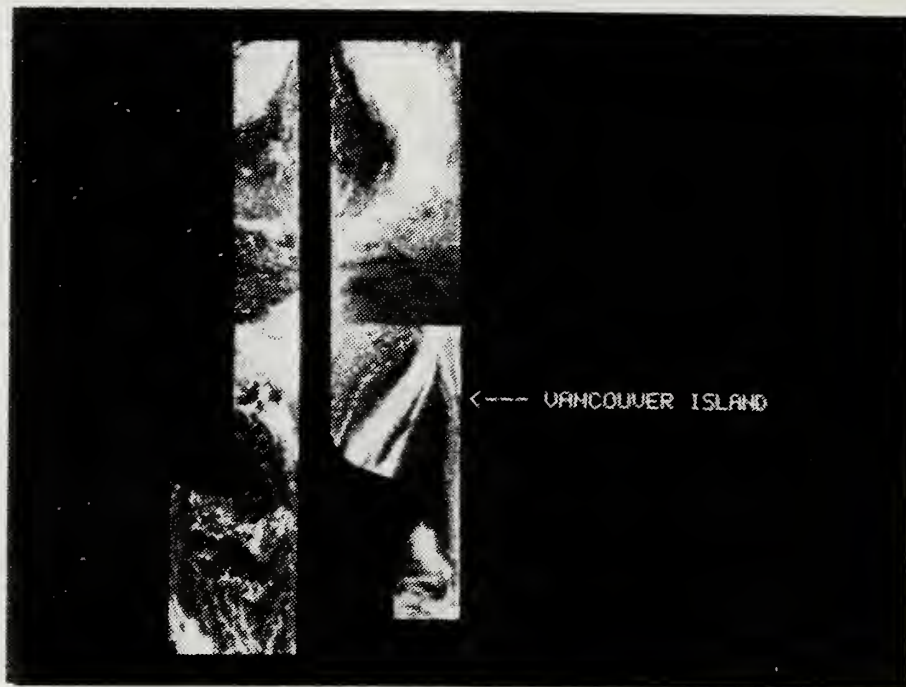


Fig. 3.2 Same as Fig. 3.1 with sunlint region deleted
40°N to 10°S, western half of image.

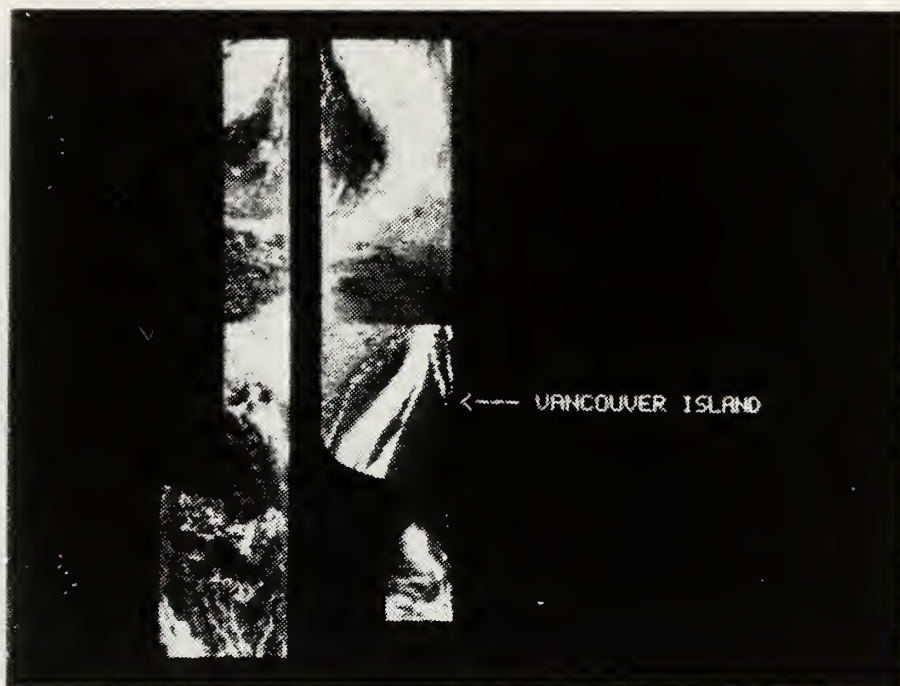


Fig. 3.3 Same as Fig. 3.1 with sunglint, land and cloud pixels deleted.

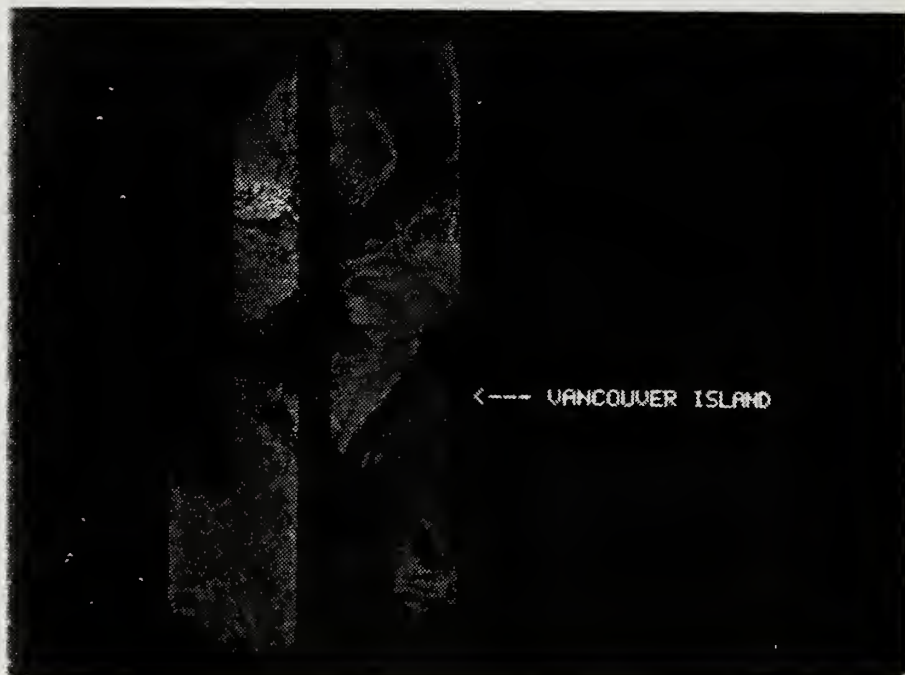


Fig. 3.4 Same as Fig. 3.1 with sunglint and clouds deleted based on channel 2 brightness value threshold test.

Second, channel 4 temperatures were used to detect thin cirrus, which is much colder than the ocean surface, but is often undetectable in channels 1 and 2. Again, a conservative approach was taken. Any channel 4 pixel value greater than 250 was eliminated due to possible contamination by cirrus.

The third check involved situations where a thick aerosol layer resulted in channel 1 and 2 brightness counts at or slightly above brightness counts representative of small fair weather cumulus clouds. It was difficult to pick out the cloudy pixels since their temperature was close to the ocean temperature. Thus these pixels were undetectable in channel 4. The ratio of channel 1 to channel 2 albedo turned out to be a good tool in these cases. Small cumulus in clear air had ratios near 1.2 whereas aerosol was at or above 1.4. Ratios in clear air over open ocean were around 1.8. Therefore 1.3 was chosen as the upper limit for the ratio value, below which it was assumed that small clouds were contaminating the scene. Table 5 shows representative ratio values for various conditions. These two tests (channel 4 and the ratio values) were applied simultaneously so that cloudless cold water regions in the far North and South Pacific Ocean would not be excluded by the channel 4 test alone and small cumulus, which were missed by channels 2 and 4 alone, would be excluded. In Fig. 3.5, it is to be noted that the clouds visible in Fig. 3.1 near 50°S are removed and the water areas near 50°N are retained. It was very difficult to eliminate the smallest cumulus elements based on these tests, especially when they laid under thick haze.

It is obvious from the preceding figures that each test by itself takes out most unwanted pixels. There is much overlap in applying the tests. Yet when applied together it is estimated that more than 95% of the unwanted pixels are deleted from the image, based on a subjective visual examination of images. The resulting image for our case study is Fig. 3.6. The haze layer now stands out clearly. A blow-up of this region is shown in Fig. 3.7.

C. STATISTICS

The statistics were computed by averaging in one degree boxes over the region. This means the area was split into a 181×101 array. In addition to mean albedos for channels 1 and 2 and their mean ratio, standard deviations of the values were calculated. A time average over the first six days (5-10 April), the second six days (20-25 April) and the entire data set was done, and the results are presented separately.

TABLE 5
 REPRESENTATIVE CHANNEL 1/CHANNEL 2
 RATIO VALUES FOR VARIOUS ATMOSPHERIC CONDITIONS

Region	Ratio value
cloud-free land	0.96
cirrus in a haze-free ocean	1.18
cumulus in a haze-free ocean	1.20
small cumulus under haze	1.50
cloud-free haze in ocean	1.59
cloud-free, haze-free ocean	1.78

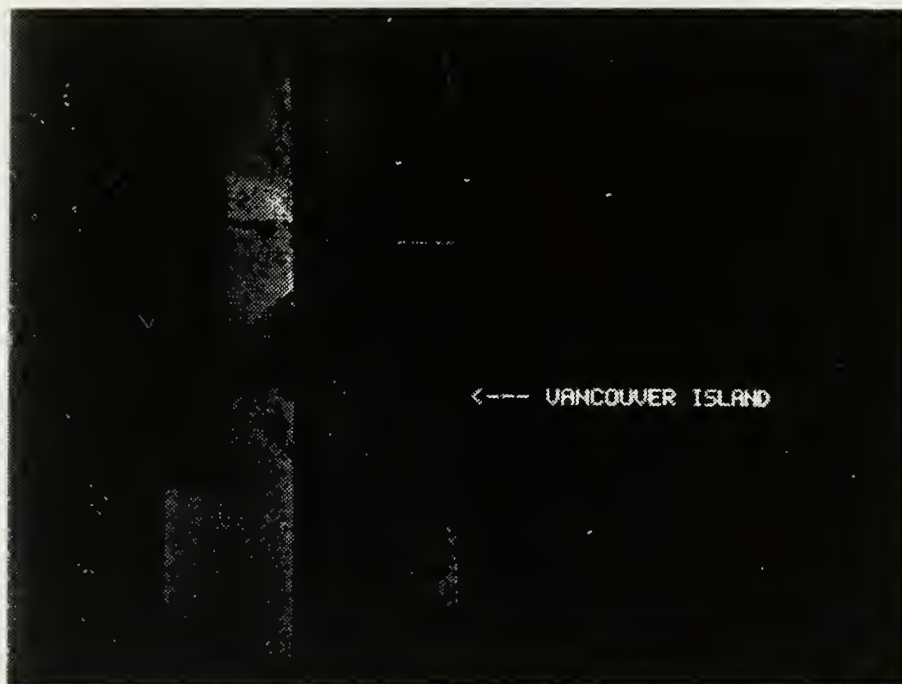


Fig. 3.5 Same as Fig. 3.1 with sunglint and clouds deleted based on channel 4 brightness value threshold and ratio value threshold tests.

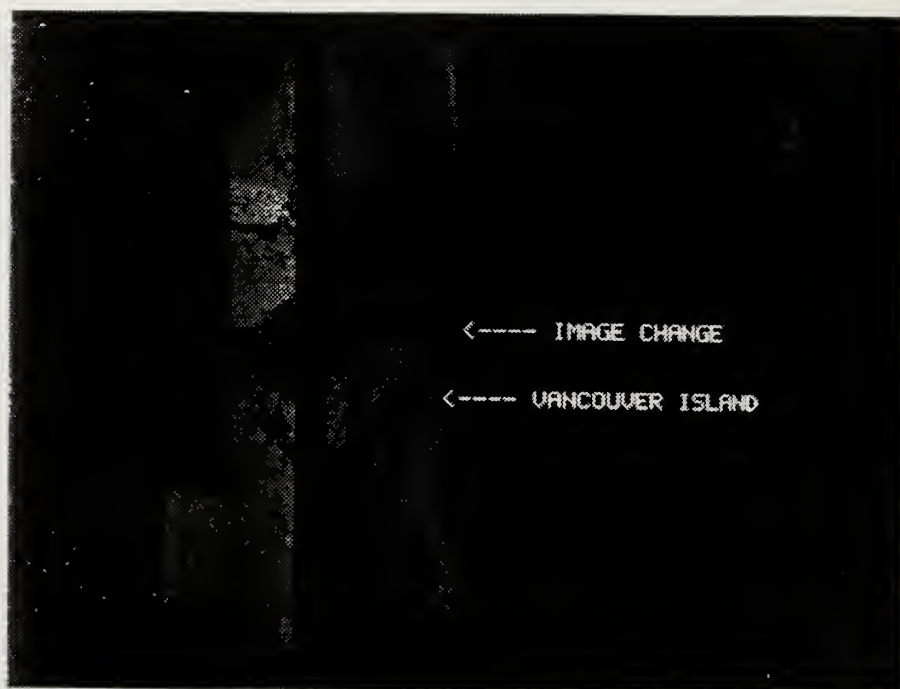


Fig. 3.6 Same as Fig. 3.1 with all contaminant tests turned on:
this image was included in climatological statistics.

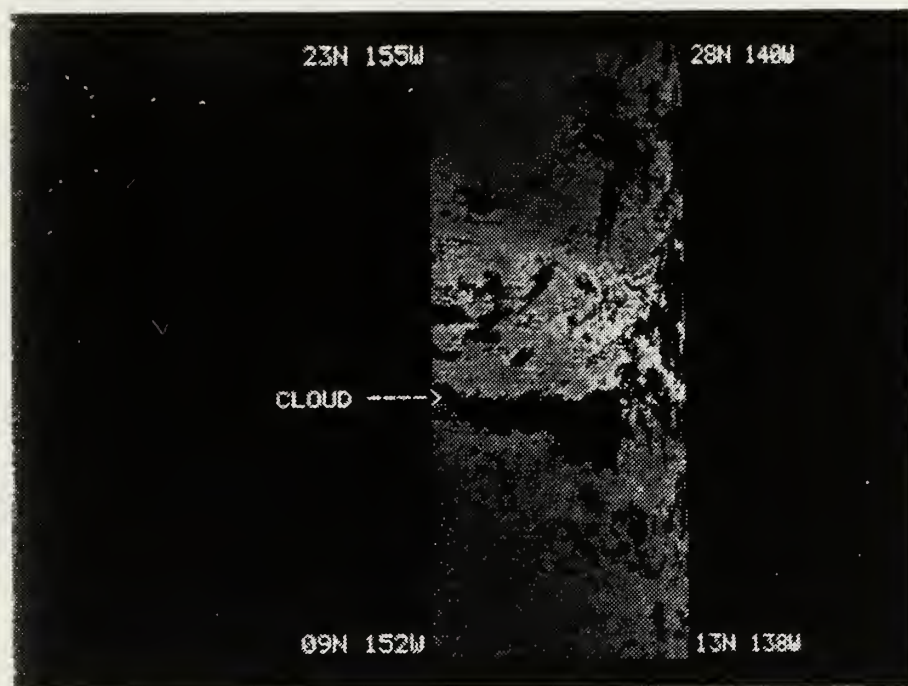


Fig. 3.7 Enlargement of a portion of Fig. 3.6:
bright strip across center of image is haze.

The number of "good" pixels (not cloudy and not in the sunglint over open ocean) was retained for each time period. Therefore in each one degree box it was known how many pixels were used in the statistics. Then, those areas of the North and South Pacific Ocean which had better data coverage, and therefore where the statistics were more reliable, could be estimated. This also gave an indication of where persistent cloudiness occurred.

It can be seen from Fig. 3.8 that the sunglint check between 40°N and 10°S , seen as generally northwest-southeast oriented strips, deleted a large number of pixels compared to the southern hemisphere. It can also be seen that adjacent overlapping satellite passes did not fill in these strips evenly. This is an artifact of the small data set used and would presumably disappear with a sufficiently large sample. Fig. 3.9 illustrates the data density for the second period. Although there is much less data than for the first six-day period, the same pattern is observed. It can be seen from the full data set coverage pattern, Fig. 3.10, that there is a dramatic increase in data south of 10°S , the sunglint strips are discernable but more evenly filled in than for the two six-day periods, and there is a paucity of data in northern and southern latitudes.

The major feature in Fig. 3.11, the channel 1 albedo for 5-10 April, is the maximum in the northern hemisphere and the minimum in the southern hemisphere. There is a minimum in the Sea of Japan and along the west coast of North America, and a maximum on both sides of Central America; one stretching north and then east across the Gulf of Mexico, the other to the southeast. The pattern in Fig. 3.12, the channel 1 albedo for 20-25 April, is similar, with the maximums near Central America expanded. Fig. 3.13 illustrates the resulting pattern for the full data set. It can be seen that there is a maximum in channel 1 albedo in the northern hemisphere and a minimum in the southern hemisphere, with distinct regional minima in the Sea of Japan, and along the west coast of North America, and regional maxima on both sides of Central America. Recall from the discussion of Table 3 that there is a critical value for the albedo, above which it is presumed aerosol scattering is dominating Rayleigh scattering; that value is approximately 2.0. Therefore, in Figs. 3.11, 3.12 and 3.13, where the values of albedo are significantly above 2.0, it is presumed that aerosol type can be inferred from the ratios of channel 1 to channel 2 albedo. Note that this is true for nearly all of the area.

The El Chichón volcano (17.3°N , 95.2°W) erupted several times between 28 March and 6 April, spewing debris into the troposphere and stratosphere. Robock and

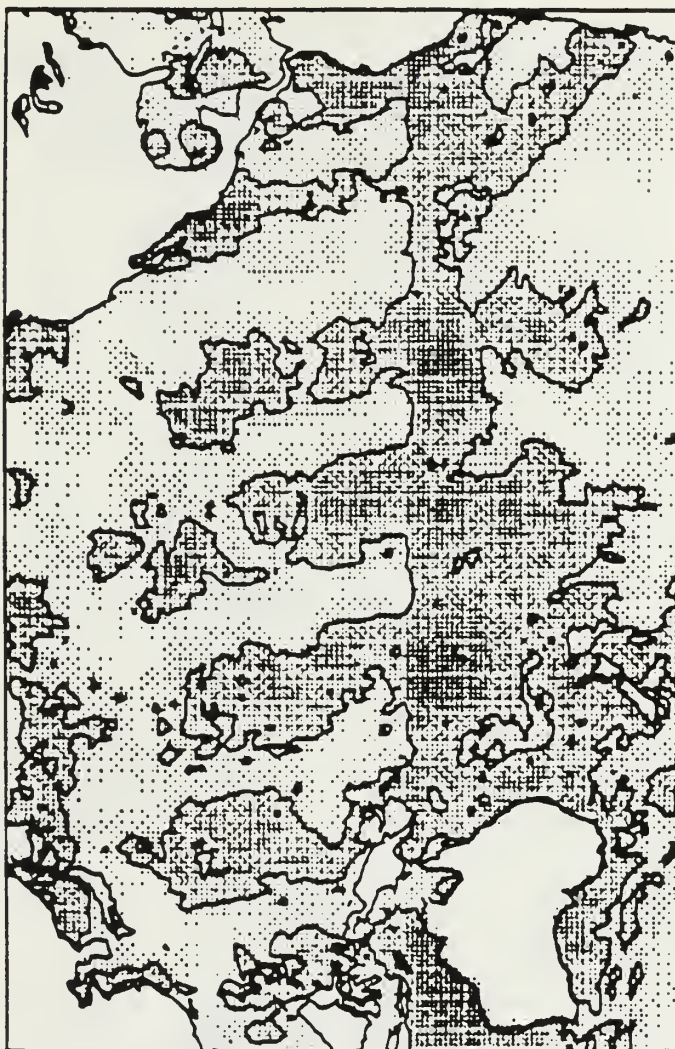
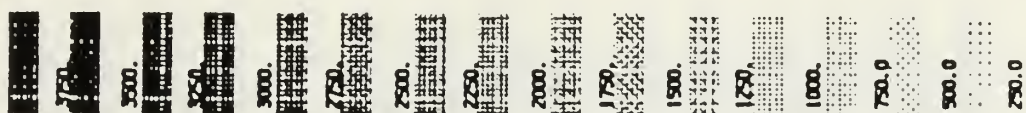


Fig. 3.8 Number of pixels used in calculating statistics for 5-10 April 1982. Areas with greater than 1000 pixels are outlined.

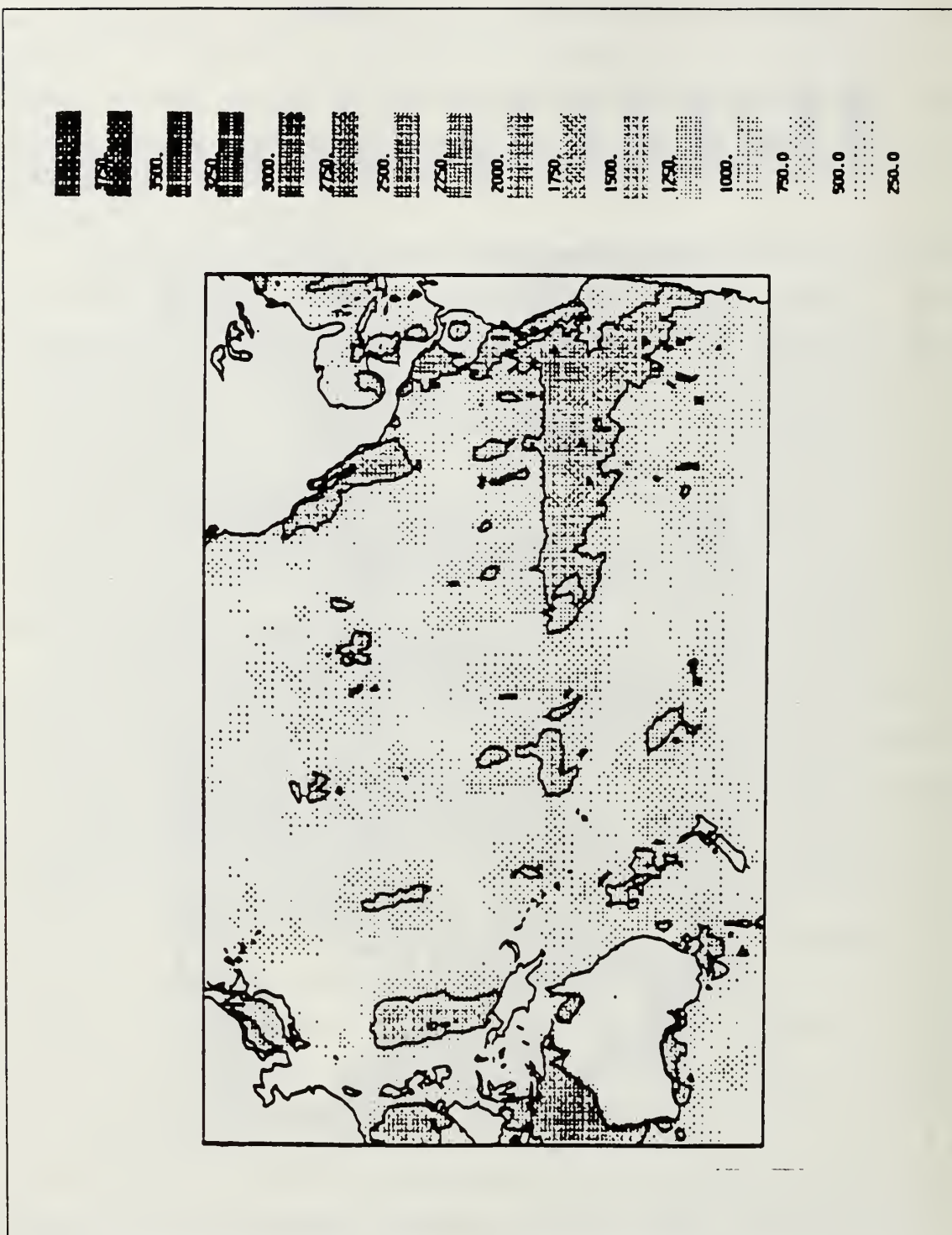


Fig. 3.9 Number of pixels used in calculating statistics for 20-25 April 1982. Areas with greater than 1000 pixels are outlined.

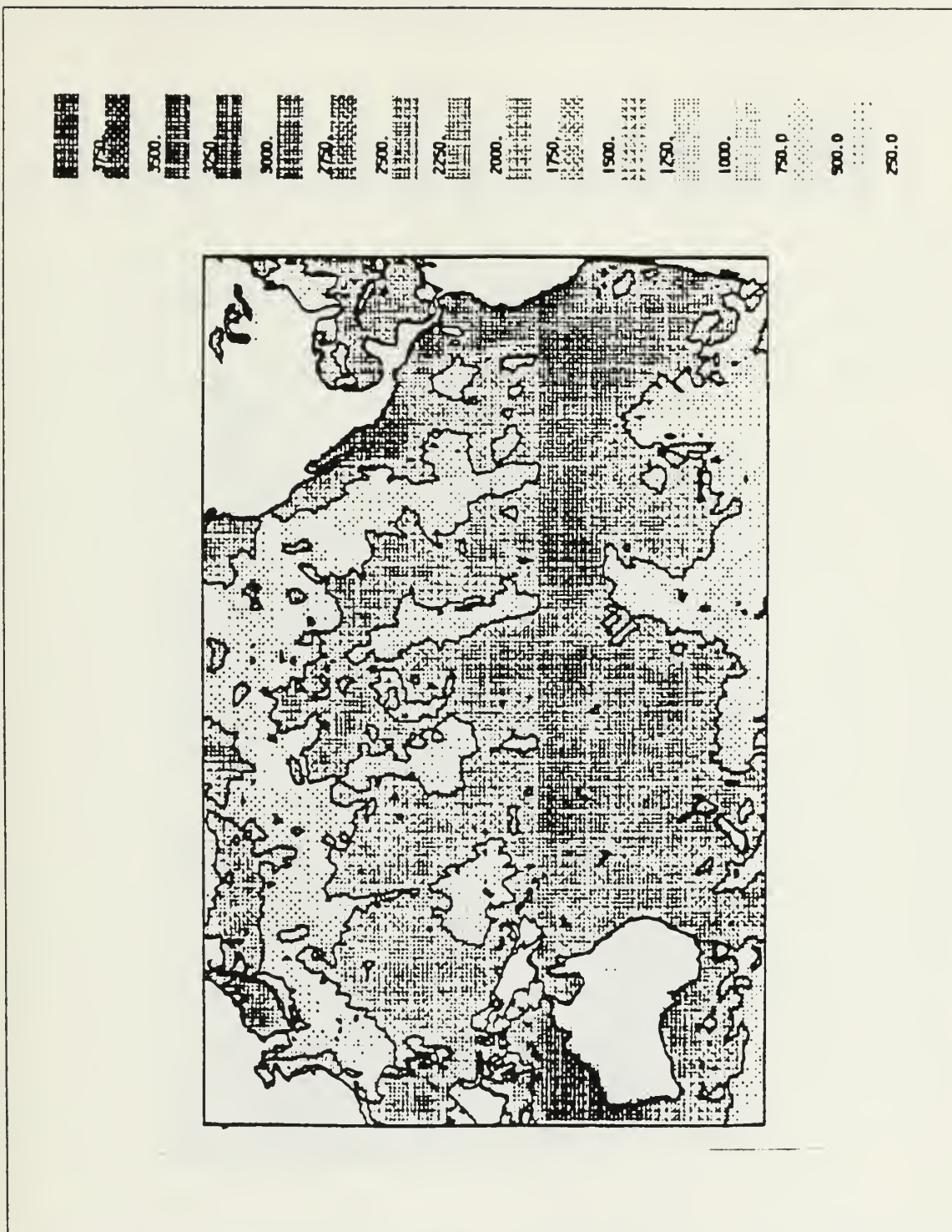


Fig. 3.10 Number of pixels used in calculating statistics for 5-10 and 20-25 April 1982. Areas with greater than 1000 pixels are outlined.

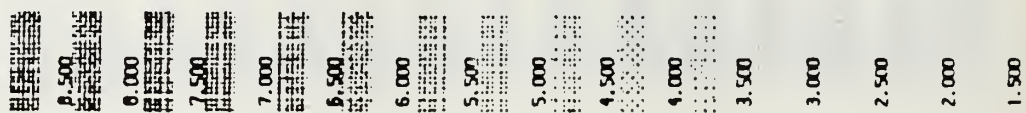


Fig. 3.11 Mean channel 1 albedo for 5-10 April 1982.
Albedos greater than 6.0% are outlined.

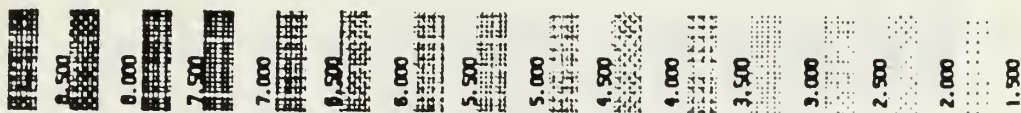


Fig. 3.12 Mean channel 1 albedo for 20-25 April 1982.
Albedos greater than 6.0% are outlined.

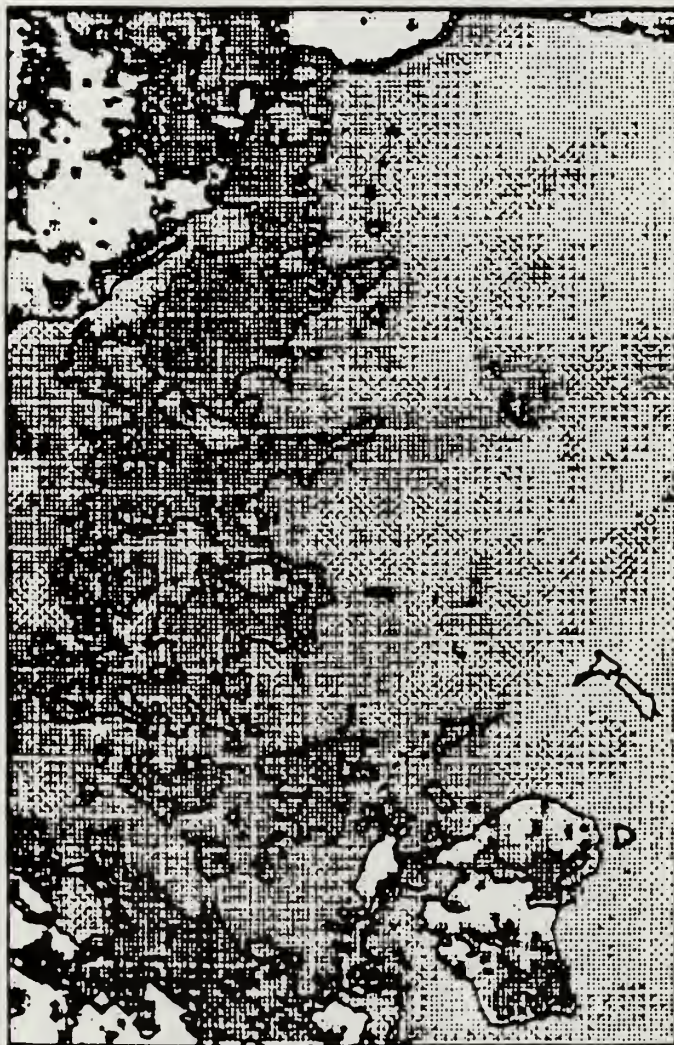
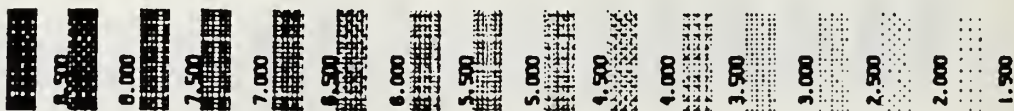


Fig. 3.13 Mean channel 1 albedo for 5-10 and 20-25 April 1982.
Albedos greater than 6.0% are outlined.

Matson (1983) mapped the circumglobal transport of the stratospheric cloud in the months after the eruptions, based on GOES and NOAA-7 visible and infrared images. Krueger (1983) estimated the positions of both stratospheric and tropospheric clouds in the days immediately following the eruptions based on Nimbus-7 total ozone mapping spectrometer data. He indicated the tropospheric debris cloud moved west while the stratospheric cloud moved east, based on observed winds from rawinsonde ascents. Sea level pressure and 500 mb analyses for 12 GMT 5 April and 12 GMT 20 April 1982 were referred to in an attempt to verify that the albedo patterns seen in Figs. 3.11, 3.12 and 3.13 could be ascribed to the El Chichón eruptions. Figs. 3.14 and 3.15 support the supposition that the El Chichón cloud is detectable in the NOAA-7 channel 1 albedo patterns of Figs. 3.11, 3.12 and 3.13.

Fig. 3.16 illustrates the channel 1 albedo standard deviation pattern for 5-10 April. It can be seen that maximum standard deviation occurs in the tropics. Fig. 3.17 illustrates the channel 1 albedo standard deviation pattern for 20-25 April. The pattern again shows highest standard deviation in the tropics. It can be seen from Fig. 3.18, the full data set channel 1 albedo standard deviation, that values are highest near the equator, and lowest near the extreme northern and southern latitudes, and along the west coast of North America. The reasoning for this pattern is not understood.

The albedo pattern in Fig. 3.19 for channel 2 during 5-10 April shows all of the same features as in channel 1 albedo (compare Fig. 3.11), except the albedo magnitude is smaller for channel 2. The northern hemisphere is a maximum, while the southern hemisphere is a minimum. There are minima in the Sea of Japan and along the North American west coast, and maxima on either side of Central America. Fig. 3.20 illustrates the channel 2 albedo pattern for 20-25 April. The pattern is again similar to channel 1 albedos for the same period (compare Fig. 3.12). The channel 2 albedo pattern for the full data set, illustrated in Fig. 3.21, is remarkably similar to the channel 1 albedo pattern (compare Fig. 3.13). Maximum albedos occur in the northern hemisphere; minimum albedos occur in the southern hemisphere. The regional maxima and minima seen in the two six-day periods are evident here. Channel 2 albedos are smaller in magnitude than channel 1 albedos.

Channel 2 albedo standard deviation for 5-10 April is shown in Fig. 3.22. Maximum values occur in equatorial regions; minimum values occur in the extreme latitudes and along the west coasts of North and Central America. Fig. 3.23 illustrates the channel 2 albedo standard deviation for 20-25 April. It shows a maximum in the

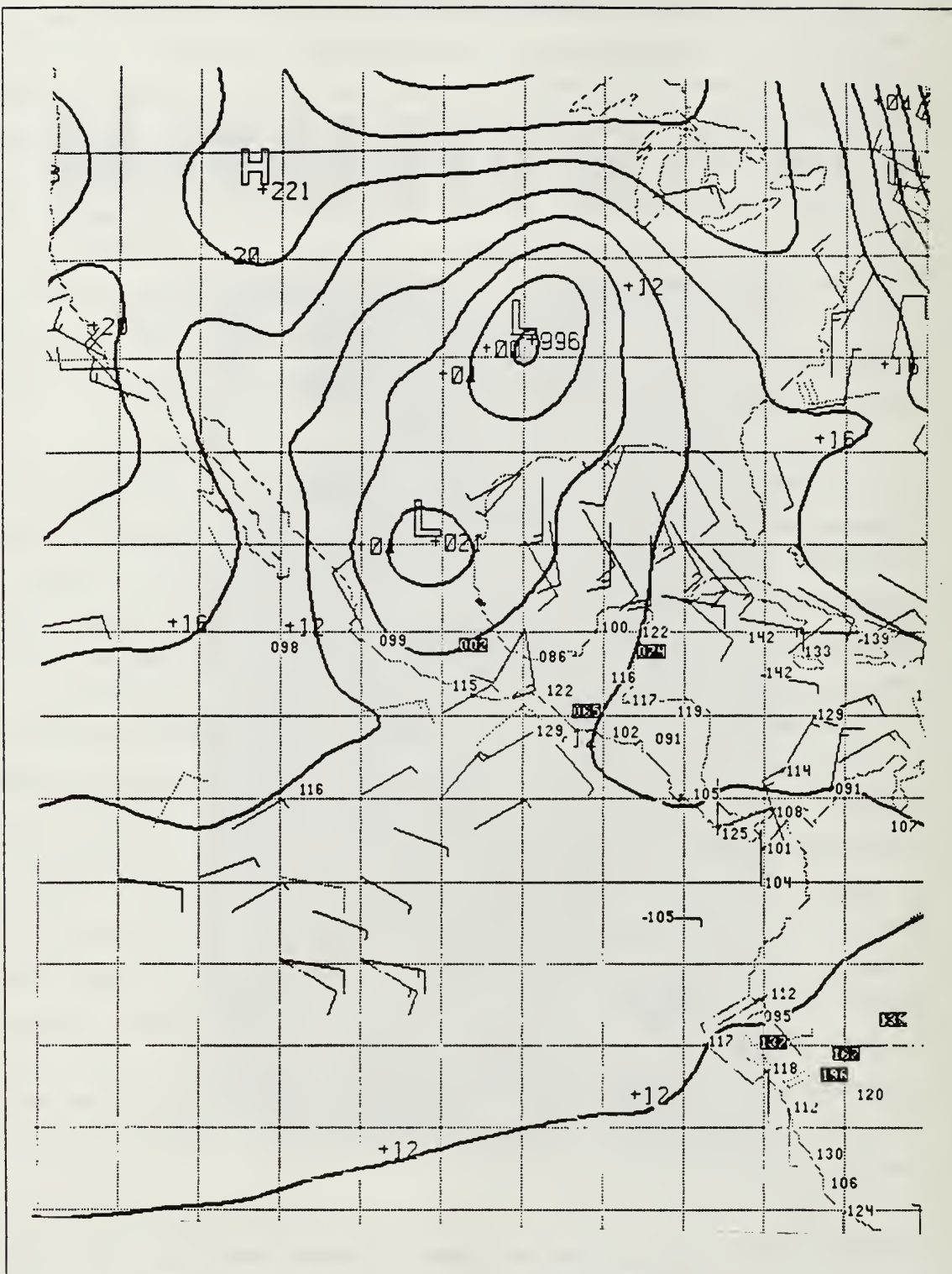


Fig. 3.14 Sea level pressure analysis for 12 GMT 05 April 1982.

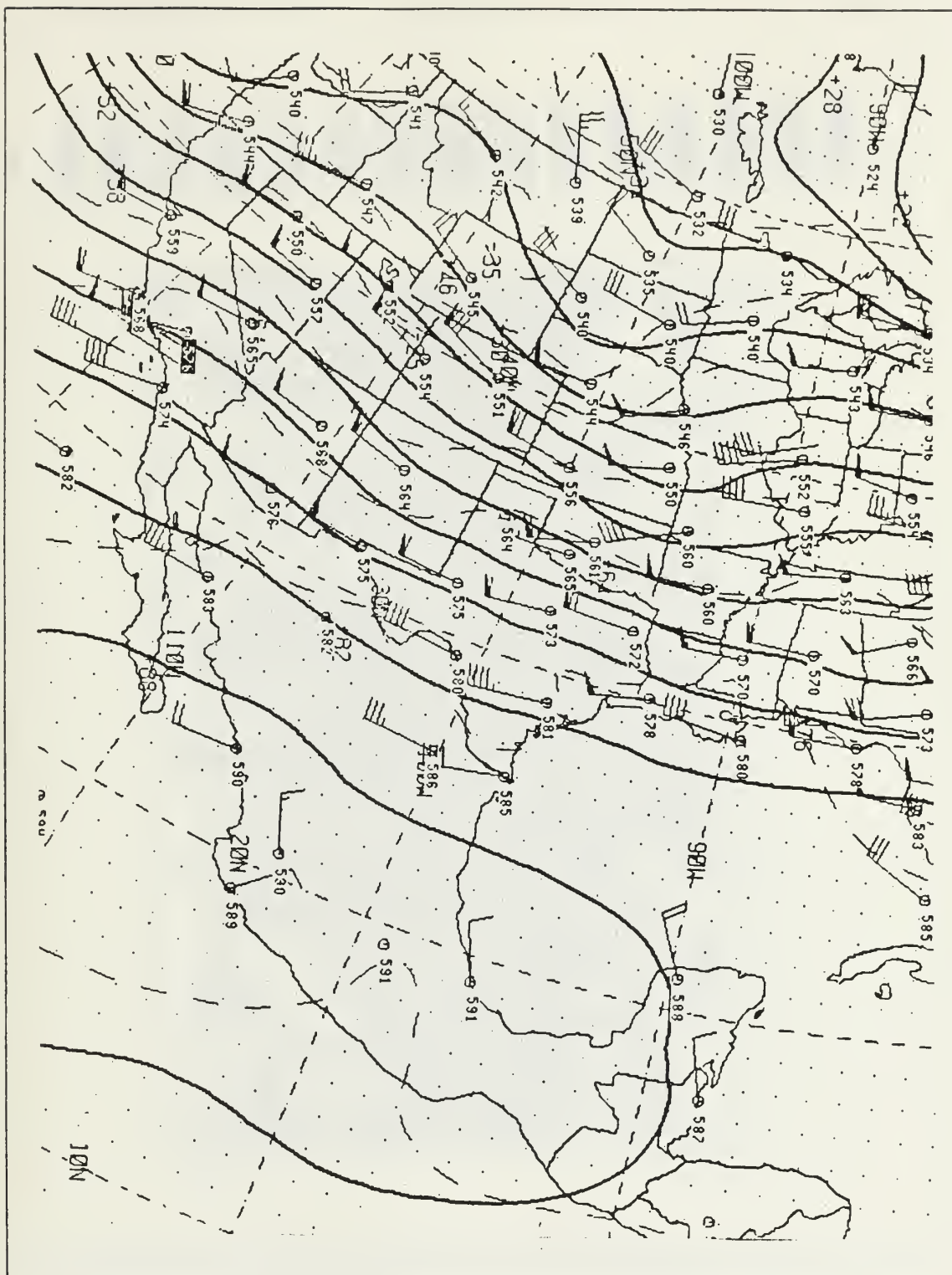


Fig. 3.15 500 mb analysis for 12 GMT 05 April 1982.

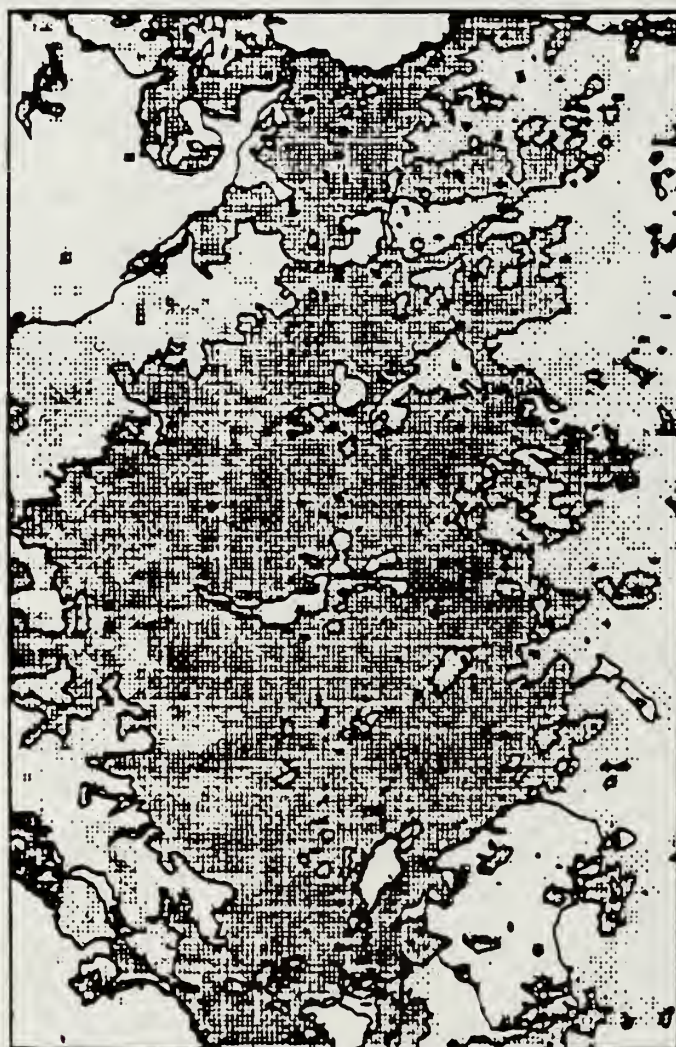
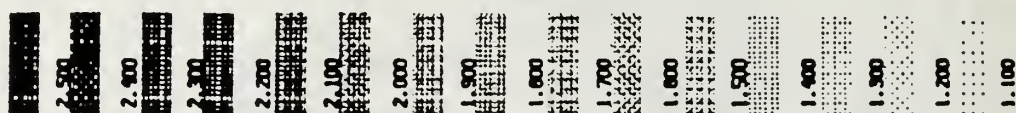


Fig. 3.16 Channel 1 albedo standard deviation for 5-10 April 1982.
Standard deviations greater than 1.5% are outlined.



Fig. 3.17 Channel 1 albedo standard deviation for 20-25 April 1982.
Standard deviations greater than 1.5% are outlined.

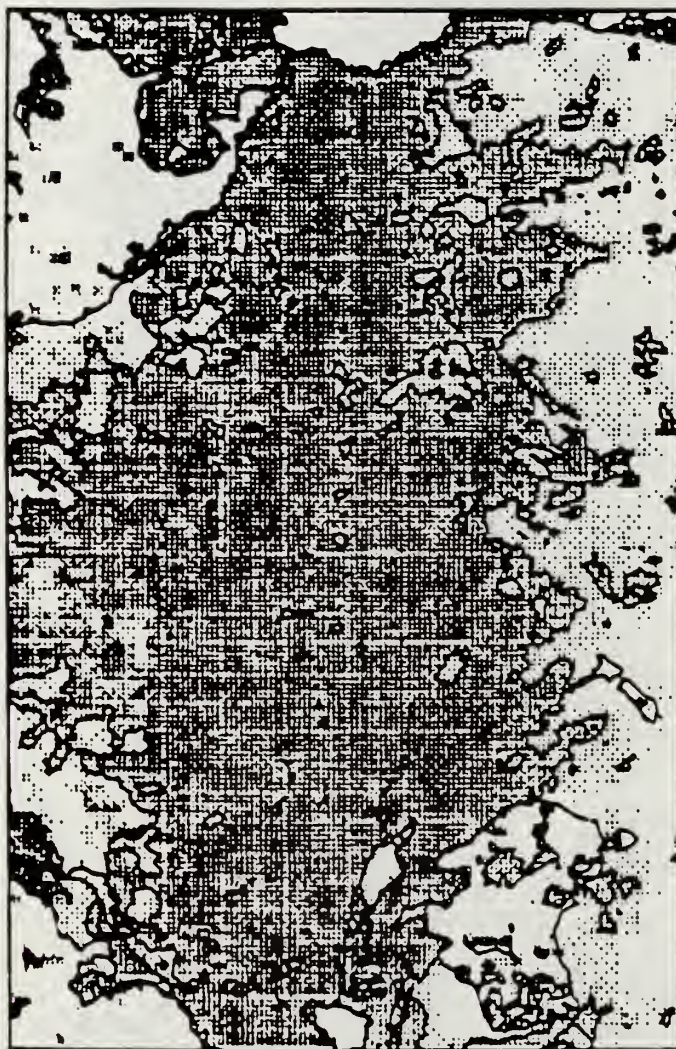
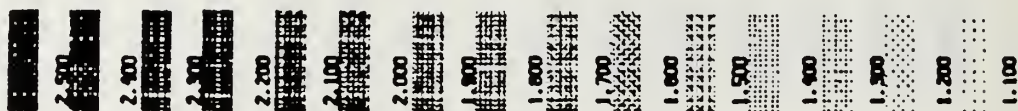


Fig. 3.18 Channel 1 albedo standard deviation for 5-10 and 20-25 April 1982. Standard deviations greater than 1.5% are outlined.



Fig. 3.19 Mean channel 2 albedo for 5-10 April 1982. Albedos less than 2.0% and greater than 4.0% are outlined.



Fig. 3.20 Mean channel 2 albedo for 20-25 April 1982. Albedos less than 2.0% and greater than 4.0% are outlined.

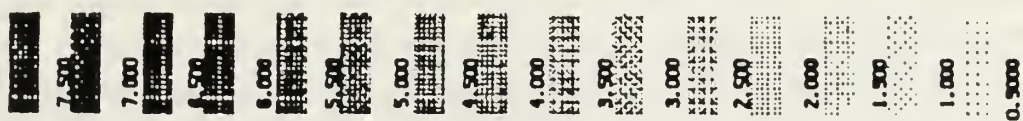


Fig. 3.21 Mean channel 2 albedo for 5-10 and 20-25 April 1982.
Albedos less than 2.0% and greater than 4.0% are outlined.

tropics, although not as extensive as for 5-10 April. It can be seen from the channel 2 albedo standard deviation pattern for the full data set, shown in Fig. 3.24, that maximum values occur near the equator, whereas minimum values occur at the extreme latitudes and along the west coasts of North and Central America.

Recall that it was difficult to remove all small cumulus clouds from the data base. This does not present a serious problem because in the marine environment, clouds cause a bias toward larger particle size; in other words, the aerosol would appear more marine in character. Ratio values would be decreased by the presence of small cumulus clouds. Having acknowledged this bias, the channel 1 to channel 2 albedo ratio pattern for 5-10 April can be seen in Fig. 3.25. There is a maximum in the tropics, with regional maxima in the East China Sea, the Sea of Japan and east of Japan, off the north, west, and south coasts of Australia, around New Zealand, and off the west coasts of Mexico and South America. Minimum values occur at the extreme latitudes, with regional minima in the southwestern Gulf of Mexico, off the east coast of Australia, and southeast of Japan. Fig. 3.26 illustrates the ratio pattern for 20-25 April. Maximum values occur in the tropics, with regional maxima in the Sea of Japan, off the northwest, south and southeast coasts of Australia, north of New Zealand, and off the west coasts of North, Central and South America. Minimum values are found at the extreme latitudes, and in the Gulf of Mexico, east of Australia and southeast of Japan. Ratio values for the full data set are illustrated in Fig. 3.27. Maximum values extend from the west coasts of North, Central and South America across the equatorial Pacific Ocean. Maxima can also be seen around and northeast of New Zealand, in the East China Sea and Sea of Japan, and off the north, west and south coasts of Australia. Minimum values occur in extreme northern and southern latitudes, the southwest Gulf of Mexico, southeast of Japan, and off the east coast of Australia.

Recall that, if an estimate for Rayleigh scattering can be made, high ratio values indicate the presence of a continental type of aerosol and low ratio values indicate a marine aerosol distribution. It can be seen from Fig. 3.27 that China, North America and Central America are apparent sources of continental aerosols in the northern hemisphere, and Australia, New Zealand and South America are apparent sources of continental aerosols in the southern hemisphere. Sea level pressure and 500 mb analyses were referred to in an effort to support this interpretation of the data. Surface winds over northern Australia were light and variable in the early days of April, while

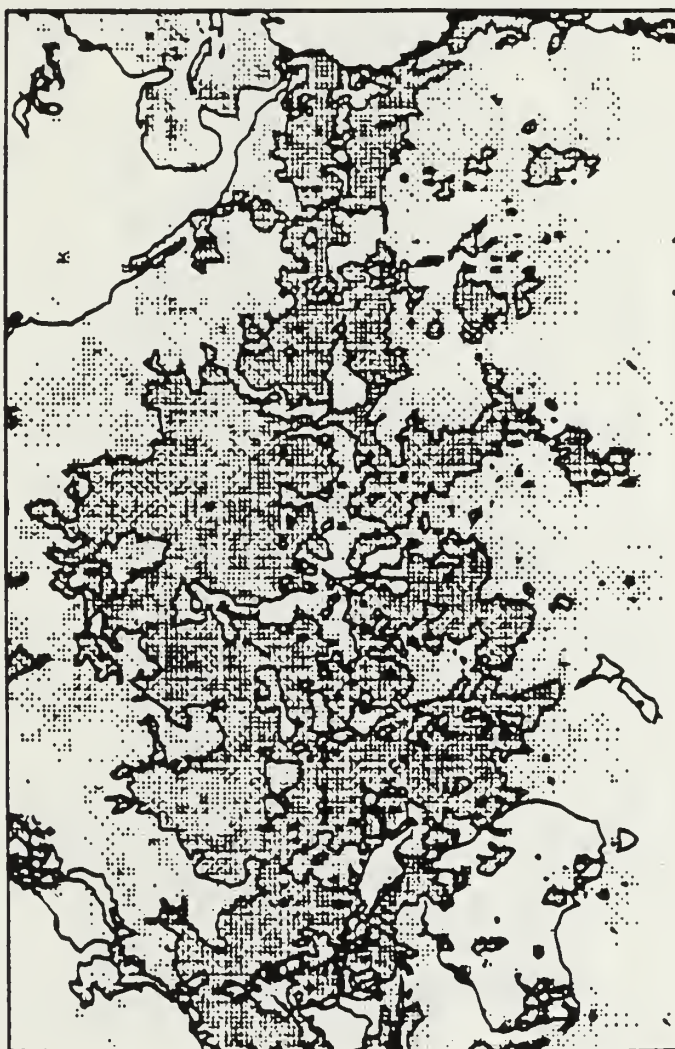
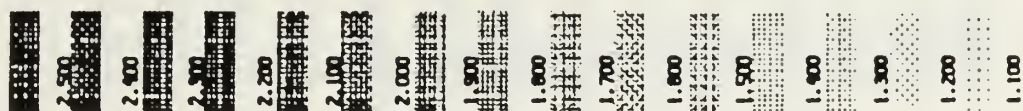


Fig. 3.22 Channel 2 albedo standard deviation for 5-10 April 1982.
Standard deviations greater than 1.5% are outlined.

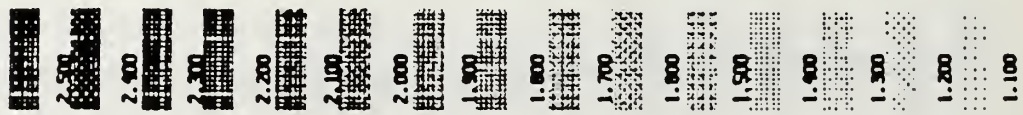


Fig. 3.23 Channel 2 albedo standard deviation for 20-25 April 1982. Standard deviations greater than 1.5% are outlined.

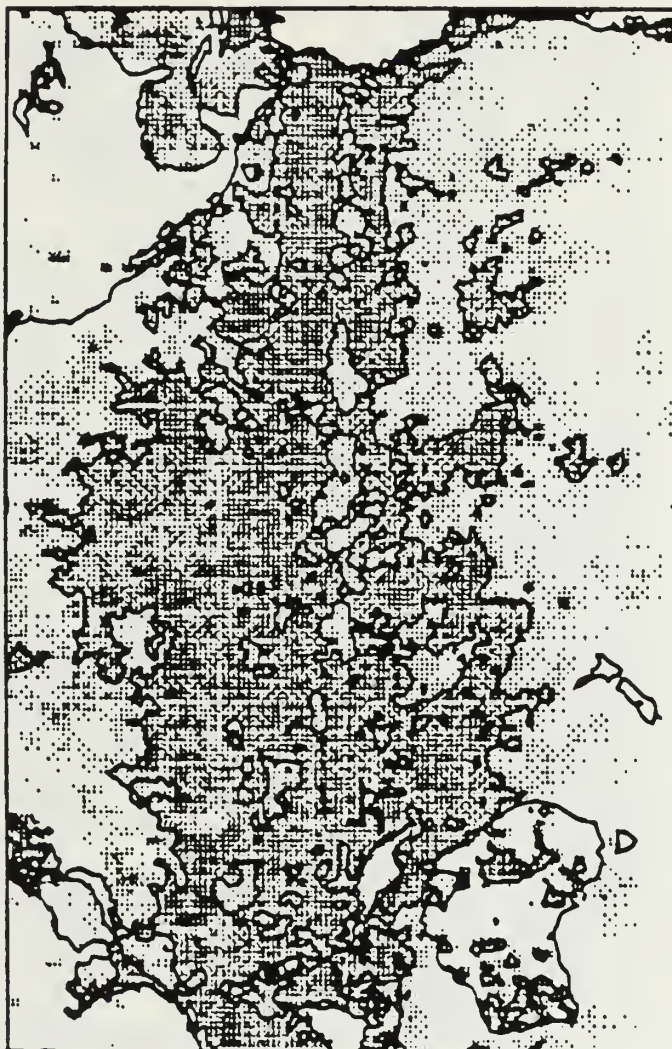


Fig. 3.24 Channel 2 albedo standard deviation for 5-10, 20-25 April 1982. Standard deviations greater than 1.5% are outlined.

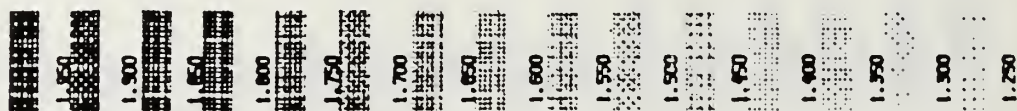


Fig. 3.25 Mean channel 1/channel 2 ratios for 5-10 April 1982.
Ratios greater than 1.6 are outlined.

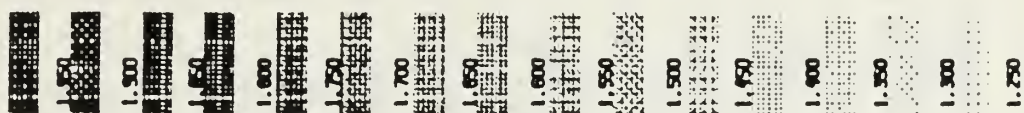


Fig. 3.26 Mean channel 1/channel 2 ratios for 20-25 April 1982.
Ratios greater than 1.6 are outlined.

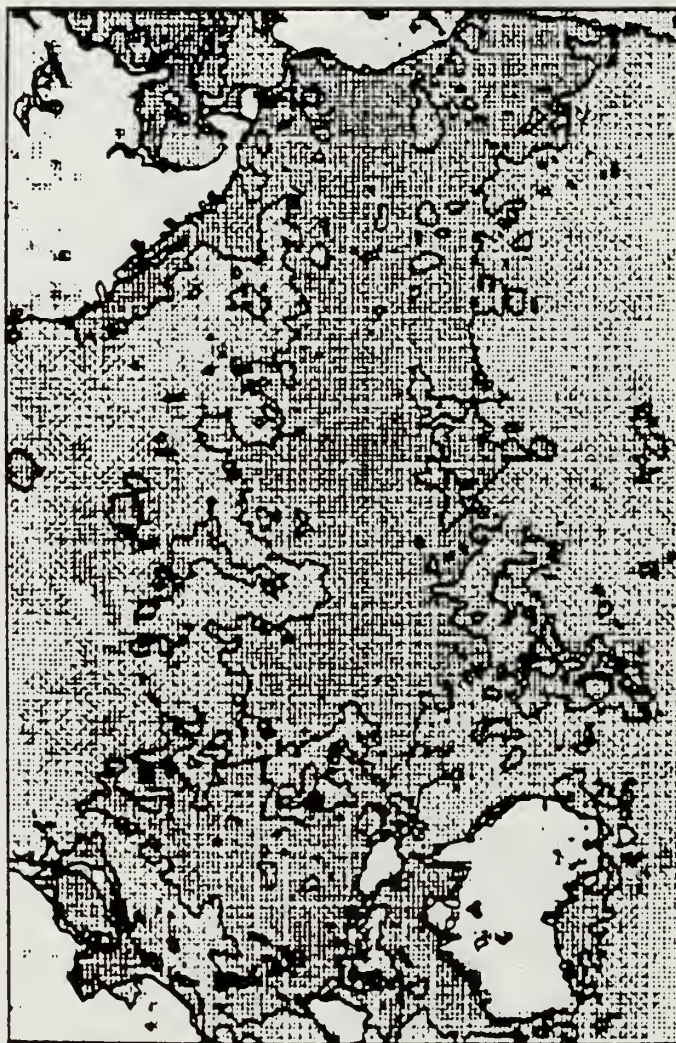
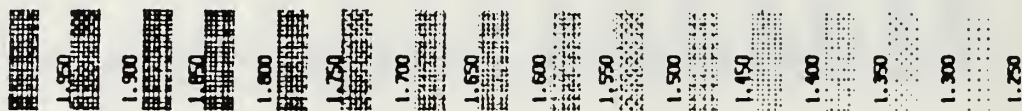


Fig. 3.27 Mean channel 1/channel 2 ratios for 5-10 and 20-25 April 1982. Ratios greater than 1.6 are outlined.

two tropical storms formed to the northeast. Later in the month easterly trade winds re-established themselves over the region. The west and south coasts of Australia were influenced by a high pressure cell that moved from the Bight to Tasmania during the month. This kept the winds off-shore on those coasts. Eastern Australia, as well as New Zealand, were affected by the two tropical storms. Both storms moved southeastward, the first becoming an intense extra-tropical storm that passed just to the north of New Zealand, the second slowly dying off the east coast of Australia. These systems kept the winds on-shore in eastern Australia and brought southerly winds of 40 kt to New Zealand on 9 and 10 April. The remainder of the month brought southeasterly winds of 15-25 kt to New Zealand. At 500 mb, winds over Australia were generally westerly and increased through the month. Over New Zealand 500 mb winds were west-southwesterly.

In the China-Japan area, a strong high pressure cell at sea level in early April moved south and weakened, allowing several lows to develop near southern Japan and move rapidly northeast. These storms brought strong west-northwesterly winds out of China and across the East China Sea and Sea of Japan while the trade winds south of Japan remained strong out of the east.

The apparent maximum of continental aerosol throughout the tropical Pacific Ocean is the most unexpected feature in the ratio pattern. The convergence of northern hemisphere northeasterly trade winds and southern hemisphere southeasterly trade winds, carrying continental aerosols from the Americas, is a possible explanation of the equatorial Pacific Ocean maximum. Time sequences and trajectory analyses must be studied to fully understand this phenomenon.

The Gulf of Mexico minimum in ratio values in the region of El Chichón is at first surprising. However, Dutton and DeLuisi (1983) have shown that the spectral response of the aerosol optical depth for the El Chichón cloud was very flat (see Fig. 3.28). A ratio of channel 1 to channel 2 albedos from an aerosol with optical depth as in Fig. 3.28 would result in low ratios.

Fig. 3.29 illustrates the ratio standard deviation pattern for 5-10 April. Maximum values occur in the tropics and East China Sea; minimum values in the southern hemisphere, southwest of North America and in the Gulf of Mexico. The 20-25 April ratio standard deviation pattern is shown in Fig. 3.30. The pattern is similar to that in Fig. 3.29, but maximum values are not as high in the tropics. It can be seen from the full data set ratio standard deviation pattern of Fig. 3.31 that

maximum values occur in the equatorial Pacific Ocean and East China Sea. Minimum values occur in the southern hemisphere, northern hemisphere except for the northwest Pacific Ocean, and southwestern Gulf of Mexico.

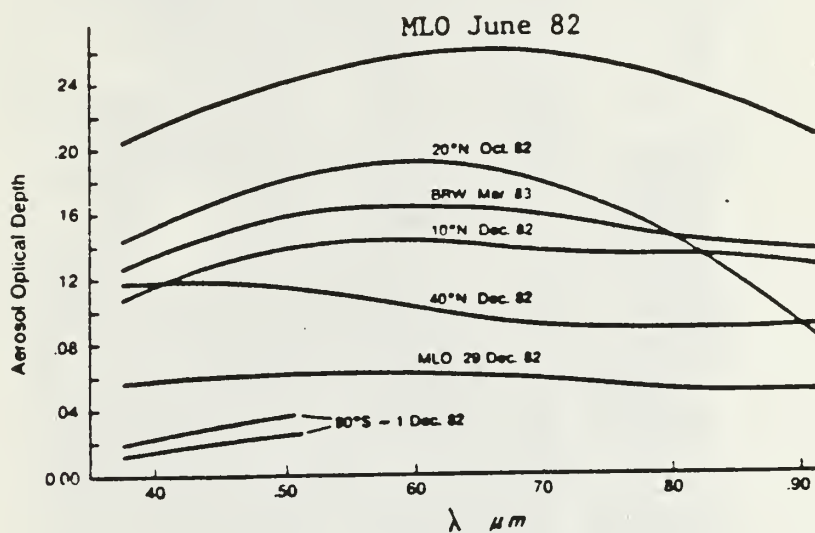


Fig. 3.28 The El Chichon component of aerosol optical depth as a function of wavelength. Curves are labelled with station or latitude and date (from Dutton and DeLuise, 1983).

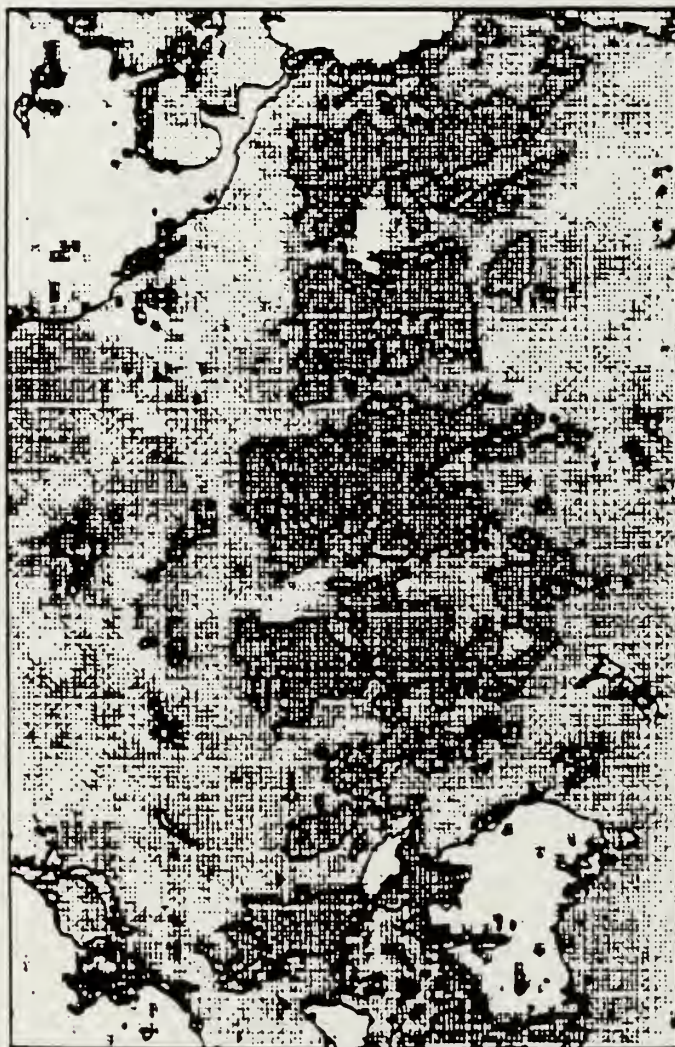
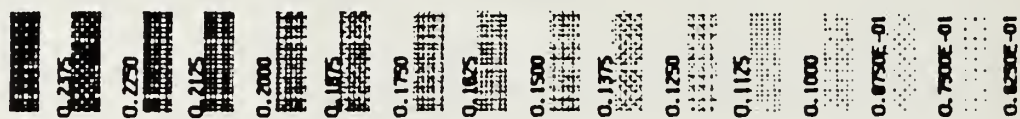


Fig. 3.29 Ratio standard deviation for 5-10 April 1982.
Standard deviations greater than 0.2 are outlined.

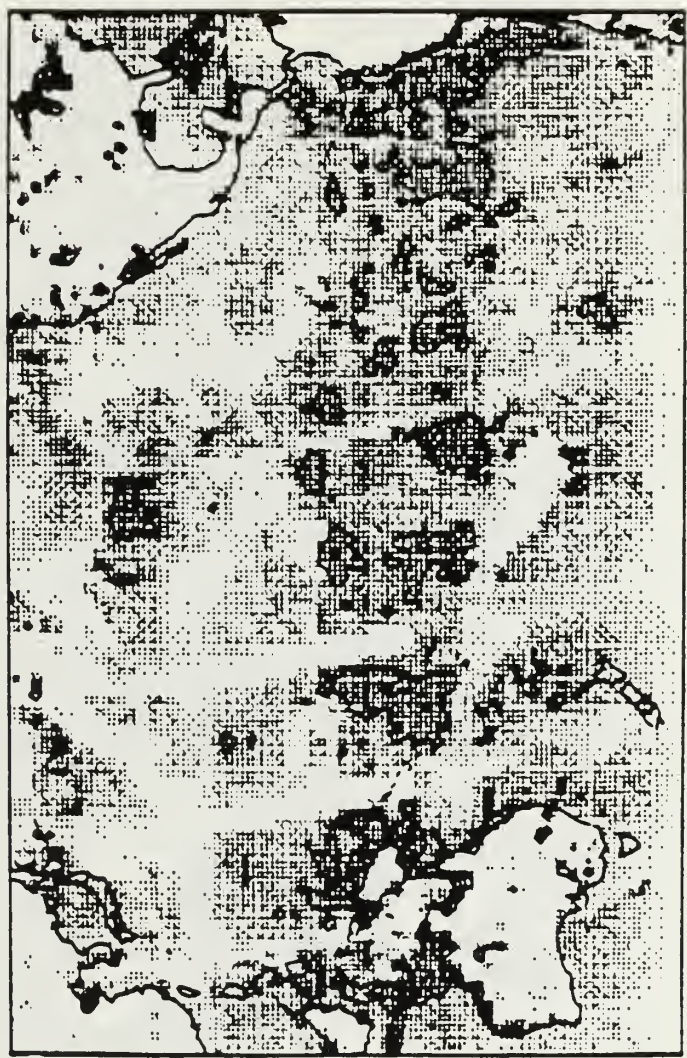
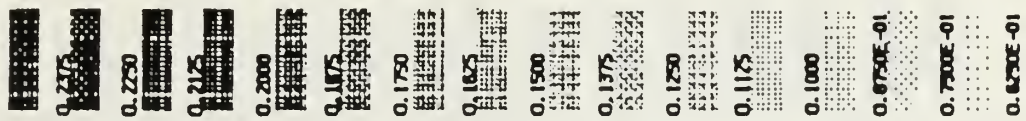


Fig. 3.30 Ratio standard deviation for 20-25 April 1982.
Standard deviations greater than 0.2 are outlined.

0.2175
 0.2250
 0.2125
 0.2000
 0.1875
 0.1750
 0.1625
 0.1500
 0.1375
 0.1250
 0.1125
 0.1000
 0.0750E-01
 0.7500E-01
 0.6250E-01

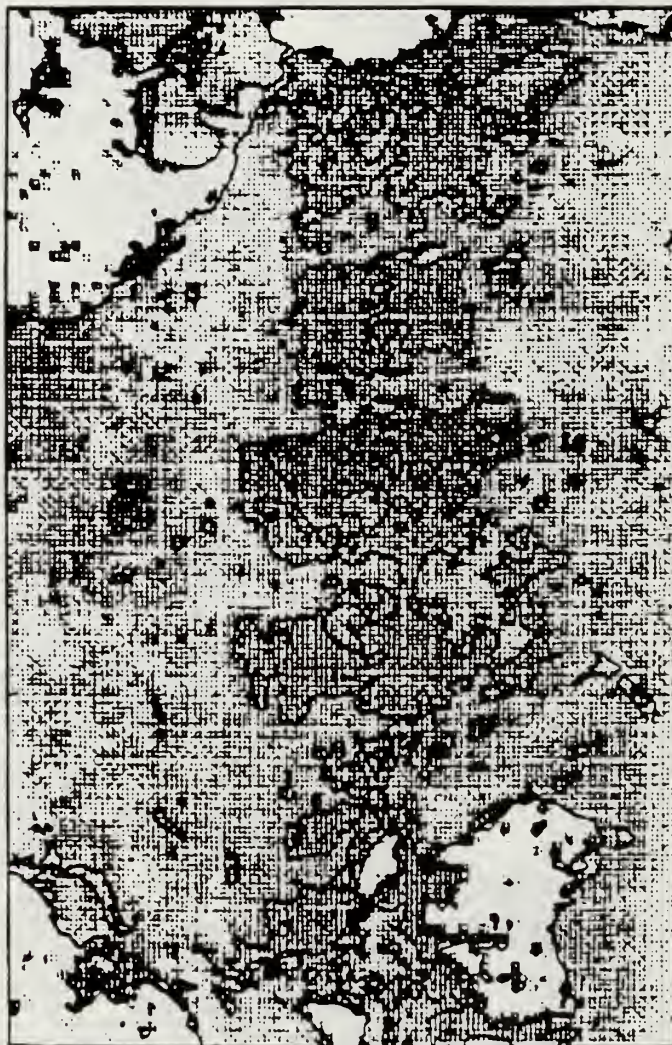


Fig. 3.31 Ratio standard deviation for 5-10 and 20-25 April 1982.
 Standard deviations greater than 0.2 are outlined.

IV. CONCLUSIONS AND RECOMMENDATIONS

A NOAA-7 AVHRR data set for 5-10 and 20-25 April 1982 was used to establish a physical basis for an aerosol climatology in the North and South Pacific Ocean. Channel 1 ($0.63\mu\text{m}$), channel 2 ($0.86\mu\text{m}$), and channel 4 ($11\mu\text{m}$) data were used to eliminate pixels that were over land or cloudy and to compute various statistics. A summary of conclusions follows:

1. In addition to using threshold values in channel 2 and 4 albedos to eliminate clouds, a new technique based on the ratio of channel 1/channel 2 albedo was developed to eliminate small fair weather cumulus that would otherwise have been included in the data set. These cloud elements are difficult to differentiate because their brightness counts in channel 2 data are equal or greater than that for heavy haze events. Their temperatures from channel 4 data are nearly equal to the sea-surface temperature. However, ratio values were less than 1.3, whereas haze events had ratios of 1.4 or greater. Therefore application of this method includes cases of heavy haze where brightness counts would be greater than the cloud detection threshold.
2. High ratio values were obtained over the equatorial Pacific Ocean, along the west coasts of North, Central and South America, in the Sea of Japan and East China Sea, off the north, west and south coasts of Australia, and around New Zealand. Low ratio values were obtained in the extreme northern and southern latitudes, southeast of Japan, the southwestern Gulf of Mexico, and off the east coast of Australia. Theory leads to the conclusion that high ratio values indicate areas of continental aerosol type, while low ratios indicate areas of marine aerosol type. This, in turn, suggests that Asia and North and Central America are sources of continental aerosol in the northern hemisphere and Australia, New Zealand and South America are sources of continental aerosol in the southern hemisphere.
3. Channel 1 and 2 albedos can be used to identify major aerosol-producing events, such as volcanic eruptions. A pattern in the albedos was linked to the El Chichón eruptions of March-April 1982, based on previous analyses of the debris cloud drift and winds from surface and upper-air data at the time.

Several improvements and further studies remain to be done. The cloud discrimination technique needs to be refined to ensure a complete elimination of clouds while keeping all cloud-free regions in the data set. The sun-earth-satellite geometry can be taken into account, correcting the cloud detection threshold for the latitudinal variation in cloud brightness. The effects of water vapor absorption on AVHRR channel 1 and 2 albedos, and, therefore, on ratio values, should be explicitly studied. The contribution of Rayleigh scattering to the total atmospheric scattering should be accounted for in the determination of ratio values. Anomalously high ratio values were found in several small areas of the study basin, both over land and at sea. Values from 5 to as high as 20 were seen. These should be investigated for physical explanations.

After a larger data base is available, time series and trajectory analyses can be done to investigate aerosol dispersion and seasonal variation. The mid-Pacific Ocean equatorial maximum in ratios also needs to be more closely investigated. Finally, further determination of sources of continental aerosols should be made.

This study represents the first step toward a satellite-derived aerosol climatology. Once fully developed, this method for establishing climatologies of aerosol amount and particularly aerosol type will be a much needed addition to studies of atmospheric radiation, the general circulation and long-term climate variations.

LIST OF REFERENCES

- Bohren, C. F., and D. R. Huffman, 1983: *Absorption and Scattering of Light by Small Particles*. John Wiley and Sons, New York, 530 pp.
- Bulfinch, S. R., 1986: Determination of the atmospheric aerosol distribution by multi-channel remote sensing techniques. M.S. thesis, Naval Postgraduate School, Monterey, CA, 87 pp.
- Carlson, T. N., 1979: Atmospheric turbidity in Saharan dust outbreaks as determined by analyses of satellite brightness data. *Mon. Wea. Rev.*, **107**, 322-335.
- , and P. Wendling, 1977: Reflected radiance measured by NOAA 3 VHRR as a function of optical depth for Saharan dust. *J. Appl. Meteor.*, **16**, 1368-1371.
- Cox, C.C., and W. Munk, 1954: Measurement of the roughness of the sea surface from photographs of the sun's glitter. *J. Opt. Soc. Am.*, **44**, 838-850.
- Durkee, P. A., 1984: The relationship between marine aerosol particles and satellite-detected radiance. Ph.D. Thesis, Colorado State University, Fort Collins, Colorado, US ISSN 0067-0340, 124 pp.
- , D. R. Jensen, E. E. Hindman, and T. H. Vonder Haar, 1986: The relationship between marine aerosol particles and satellite-detected radiance. *J. Geophys. Res.*, **91(D3)**, 4063-4072.
- Dutton, E., and J. DeLuise, 1983: Optical thickness features of the El Chichon stratospheric debris cloud. *Fifth Conference on Atmospheric Radiation*, American Meteorological Society, 361-363.
- Erickson, D. J., J. T. Merrill, and R. A. Duse, 1986: Seasonal estimates of global atmospheric sea-salt distributions. *J. Geophys. Res.*, **91(D1)**, 1067-1072.
- Fett, R. W., and R. G. Isaacs, 1979: Concerning cause of 'anomalous gray shades' in DMSP visible imagery. *J. Appl. Meteor.*, **18**, 1340-1352.
- Fleagle, R. G., and J. A. Businger, 1980: *An Introduction to Atmospheric Physics*. Academic Press, New York, 432 pp.
- Griggs, M., 1975: Measurements of atmospheric aerosol optical thickness over water using ERTS-1 data. *J. Air Pollut. Control Assoc.*, **25**, 622-626.
- , 1979: Satellite observations of atmospheric aerosols during the EOMET cruise. *J. Atmos. Sci.*, **36**, 695-698.
- , 1983: Satellite measurements of tropospheric aerosols. *Adv. Space Res.*, **2(5)**, 109-118.

- Hänel, G., 1976: The properties of atmospheric aerosol particles as functions of the relative humidity at thermodynamic equilibrium with the surrounding moist air. In *Advances in Geophysics*, 19, edited by H. E. Landsberg and J. Van Mieghen, Academic Press, New York, 73-188.
- Iwasaka, Y., H. Minoura, and K. Nagaya, 1983: The transport and spatial scale of asian dust-storm clouds: A case study of the dust-storm event of April 1979. *Tellus*, 35B, 189-196.
- Kidwell, K. B., 1984: *NOAA Polar Orbiter Data Users Guide*. National Environmental Satellite Data, and Information Service, Washington, D.C.
- Krueger, A. J., 1983: Sighting of El Chichon sulfur dioxide clouds with the Nimbus-7 total ozone mapping spectrometer. *Science*, 220, 1377-1379.
- Liou, K. N., 1980: *An Introduction to Atmospheric Radiation*. Academic Press, New York, 392 pp.
- McCartney, E. J., 1976: *Optics of the atmosphere: scattering by molecules and particles*. J. Wiley, New York, 408 pp.
- Meszaros, A., and K. Vissy, 1974: Concentration, size distribution and chemical nature of atmospheric aerosol particles in remote oceanic areas. *Aerosol Science*, 5, 101-109.
- Norton, C., F. Mosher, B. Hinton, D. Martin, D. Santek and W. Kuhlow, 1980: A model for calculating desert aerosol turbidity over the oceans from geostationary satellite data. *J. Appl. Meteor.*, 19, 633-644.
- Quenzel, H., 1984: Scattering, absorption, emission and radiative transfer in the atmosphere. In *Optical Remote Sensing of Air Pollution*, edited by P. Camagni and S. Sandroni, Elsevier Science Publishers B.V., Amsterdam, 1-25
- , 1984: Principles of remote sensing techniques. In *Optical Remote Sensing of Air Pollution*, edited by P. Camagni and S. Sandroni, Elsevier Science Publishers B.V., Amsterdam, 27-43.
- Ramsey, R. C., 1968: Study of the remote measurement of ocean color. Final report, TRW, NASW-1658.
- Robock, A., and M. Matson, 1983: Circumglobal transport of the El Chichon volcanic dust cloud. *Science*, 221, 195-197.
- Shenk, W. E., and R. J. Curran, 1974: The detection of dust storms over land and water with satellite visible and infrared measurements. *Mon. Wea. Rev.*, 102, 830-837.
- Shettle, E. P. and R. W. Fenn, 1979: Models for the aerosols of the lower atmosphere and the effects of humidity on their optical properties. *Tech. Rep. AFGL-TR-79-0214*, Air Force Geophys. Lab., Hanscomb Air Force Base, Mass.
- Takashima, T., and Y. Takayama, 1983: Investigation of the atmospheric aerosols by the visible and IR channels of the AVHRR radiometer on NOAA-6. *Adv. Space Res.*, 2, 95-104.

Woodcock, A. H., 1953: Salt nuclei in marine air as a function of altitude and wind force. *J. Meteorol.*, **10**, 362-371.

World Climate Research Programme, 1986: A preliminary cloudless standard atmosphere for radiation computation. *WCP-112, WMO/TD-No.24*.

INITIAL DISTRIBUTION LIST

		No. Copies
1.	Defense Technical Information Center Cameron Station Alexandria, VA 22304-6145	2
2.	Library, Code 0142 Naval Postgraduate School Monterey, CA 93943-5002	2
3.	Chairman (Code 63Rd) Department of Meteorology Naval Postgraduate School Monterey, CA 93943	1
4.	Chairman (Code 68Tm) Department of Oceanography Naval Postgraduate School Monterey, CA 93943	1
5.	Professor P. A. Durkee (Code 63De) Department of Meteorology Naval Postgraduate School Monterey, CA 93943	20
6.	Professor D. W. Thomson (Code 63Th) Department of Meteorology Naval Postgraduate School Monterey, CA 93943	1
7.	LCDR Frederick R. Pfeil 2633 Zastrow Rd. Hartland, WI 53029	2
8.	Director Naval Oceanography Division Naval Observatory 34th and Massachusetts Avenue NW Washington, DC 20390	1
9.	Commander Naval Oceanography Command NSTL Station Bay St. Louis, MS 39522	1
10.	Commanding Officer Naval Oceanographic Office NSTL Station Bay St. Louis, MS 39522	1
11.	Commanding Officer Fleet Numerical Oceanography Center Monterey, CA 93943	1
12.	Commanding Officer Naval Ocean Research and Development Activity NSTL Station Bay St. Louis, MS 39522	1
13.	Commanding Officer Naval Environmental Prediction Research Facility Monterey, CA 93943	1

- | | | |
|-----|---|---|
| 14. | Chairman, Oceanography Department
U.S. Naval Academy
Annapolis, MD 21402 | 1 |
| 15. | Chief of Naval Research
800 N. Quincy Street
Arlington, VA 22217 | 1 |
| 16. | Office of Naval Research (Code 420)
Naval Ocean Research and Development Activity
800 N. Quincy Street
Arlington, VA 22217 | 1 |
| 17. | Scientific Liason Office
Office of Naval Research
Scripps Institution of Oceanography
La Jolla, CA 92037 | 1 |
| 18. | Dr. Paul F. Twitchell
Code 1244
Office of Naval Research
800 North Quincy St.
Arlington, VA 22217-5000 | 1 |

183

18070

2

DUDLEY KNOX LIBRARY
NAVAL POSTGRADUATE SCHOOL
MONTEREY, CALIFORNIA 93945-5002

Thesis

P46168 Pfeil

c.1

Developing a physical
basis for an aerosol cli-
matology of the Pacific
Ocean.

Thesis

P46168 Pfeil

c.1

Developing a physical
basis for an aerosol cli-
matology of the Pacific
Ocean.

thesP46168

Developing a physical basis for an aeros



3 2768 000 70951 3

DUDLEY KNOX LIBRARY